Anales Acad. Nac. de Cs. Ex., Fís. y Nat., tomo 59 (2017): 59-93.

NANOSTRUCTURED MATERIALS
Synthesis, Characterization, Properties, Applications

Noemí Elisabeth Walsöe de Reca

CINSO (Centro de INvestigaciones en SOlidos) CITEFA-CONICET
San Juan Bautista de La Salle 4397, Villa Martelli,
(B1603ALO) Buenos Aires, Argentina
(walsoe@citefa.gov.ar)

Abstract

In this review, some aspects of the Project: "Nanostructured Materials" developed at CINSO-CONICET-CITEFA from more than ten years ago are considered. At first, nanomaterials are defined and references if their amazing properties are reported. Afterwards, different synthetic methods are mentioned, particularly, the synthesis of ionic conducting and semiconductor nanoceramics and techniques used for their characterization are reported. With regards to the study of the nanostructured materials properties, two interesting subjects were selected: the retention of metastable phases and the enhancement of the ionic conductivity related to the crystallite size decrease in nanoceramics. Finally, among the varied applications of nanostructured materials, two original developments are described: the application of nanosemiconductors in gas sensors and that of nanoceramics to build fuel cells of the type IT-SOFC (Solid Oxide Fuell Cells).

Key words: Nanostructured materials, synthesis, characterization, applications, gas sensors, fuel cells.

Resumen

Materiales nanoestructurados. En este trabajo de revision se tratan algunos aspectos del proyecto de "Materiales Nanoestructurados" que se desarrolla en el CINSO-CONICET-CITEFA desde hace más de una década. En primer lugar, se definen los nanomateriales y se comentan algunas razones de sus sorprendentes propiedades. Luego, se mencionan diferentes métodos de síntesis, particularmente la síntesis de nanocerámicos de conducción iónica y de semiconductores y las técnicas empleadas para su caracterización. En cuanto a los estudios de las propiedades de los materiales nanoestructurados se han seleccionado dos temas de interés: la retención de fases metaestables y el aumento de la conductividad iónica en relación con la disminución del tamaño de cristalita de los nanocerámicos. Finalmente, se describen dos aplicaciones de esos materiales que han generado sendos desarrollos originales: la aplicación de nanosemiconductores en sensores de gases y la de nanocerámicos en la construcción de celdas de combustible de tipo IT-SOFC (Solid Oxide Fuell Cells).

Palabras clave: Materiales nanoestructurados, síntesis, caracterización, aplicaciones, sensores de gases, celdas de combustible.

1. Introduction

Nanomaterials are systems containing particles with one dimension in the nanometer (10^{-9} meter) regime. *Nanotechnology* deals with materials or structures in nanometer scales and it is defined as the design, fabrication and application of nanostructures or nanomaterials and the fundamental understanding of the relationships between physical properties or phenomena and material dimensions. *Micro-electromechanical systems (MEMS) and lab-on-a chip* are also considered as nanotechnology [1]. There are many definitions used by people working in nanotechnology, to define the field and these defi-

nitions are true to certain specific field-areas, but none of them covers the full spectrum of nanotechnology. This fact reflects that it only covers a broad spectrum of research field, requiring true interdisciplinary and multidisciplinary efforts. Currently there is intense interest of biologists, chemists, physicists and engineers in the application of these materials and the so-called nanotechnology is sometimes referred as "the next industrial revolution" [1]. The reason for the interest is the unusual properties, very often with useful applications, exhibited by these materials when compared to their bulk counterparts [2-6]. Only very few examples will be considered here: among the physical properties distinctively different from that of bulk, it is possible to mention that crystals in the nanometer scale have a low melting point (temperature differences as large as 1000 °C), sintering at lower temperatures and reduced lattice constants, metastable phases in nanoceramics systems can be retained at lower temperature, ferroelectrics and ferromagnetics may lose ferroelectricity or ferromagnetism when the materials are shrunk to the nanometer scale, bulk semiconductors become isolators when their characteristic dimension is sufficiently small.

In nanostructured systems, the origin of the unusual properties lies in two facts: I) the dimension of the particles is similar or even smaller than the critical length for certain phenomena, like the de Broglie wavelenght for the electron, the distance required to form a Frank-Reed dislocation loop, the thickness of a space-charge layer, the mean free path of electrons, the maximum size of a magnetic domain, etc.; II) surface effects dominate the thermodynamics and energetics of the particles like crystal structure, reactivity, surface morphology, etc. The first of these facts leads, for ex., to special electric properties in nanostructured ionic materials and in nanosemiconductors to special electrical, magnetic and optical properties and the possibility of quantum dots devices. The second factor can lead to nanocrystals adopting different morphologies with regards to bulk crystals with different exposed lattice planes leading to an astonishing surface chemistry [7, 8] and catalytic activity [9, 10].

The objectives of this article are to introduce the sequential steps of the Nanostructured Materials Project at CINSO-CITEFA-CONICET. At first, the synthesis and characterization of nanostructured materials is described in the **Experimental Methodology** paragraphs. These items will be focused, in general, on the usual synthesis and characterization methods of nanomaterials and, particularly, they will refer to *nanostructured inorganic solids*, mainly ionics and semiconductors, synthesised, characterized and applied at CINSO from 1992. In **Research** paragraphs, results on synthesis and characterization of these nanomaterials will be discussed and two particular research subjects on: Metastable Phases Retention and Anomalous Diffusion in Nanostructured Electrolytes will be considered, analysing the properties useful for later applications in gas sensors and fuel cells. In the **Applications** paragraph only two types of devices (gas sensors and fuel cells) will be described because of the actual advancement degree of these developments. The reasons and advantages of choosing nanostructured materials for their building will be discussed.

2. Experimental methodology

2.1. *Synthesis of Nanostructured Materials*

Synthesised nanoceramic materials at CINSO include solid ionics for electrolytes and electrode materials (mainly nanostructures: perovskites nanotubes and mesoporous materials) to be used in solid oxide fuel-cells and semiconductors for gas sensors and optoelectronic devices.

Only few of the numerous techniques [11-13] to synthesize nanopowders of ceramic materials will be considered here, classifying them by the preparation process:

- Synthesis: starting from a *gaseous phase* [14-16] includes plasma, laser-ablation, spray-pyrolisis and electro-explosion, being the most used the RF or CC plasma technique. It is possible to synthesise a wide variety of nanomaterials and, as temperatures of processes are considerably high, not only ceramics can be prepared but also refractory materials. Even though, the laser-ablation enables to obtain practically any nanomaterial, as this technique is a mixture of physical erosion and evaporation, it results very slow and, consequently, it is mainly confined to research work. The gel-combustion technique, which can be classified inside the same process type was intensively used at CINSO to synthesise nanoceramics [17-18] and nanosemiconductors [19, 21]. This method is based on the gel formation and later combustion of nitrates of the chosen metals with an organic fuel (glycine, urea, lysine, citric acid, etc.) [22, 23]. The combustion process is due to the exothermic redox reaction among the oxidizing ions and the reducing fuel. The vigorous gases liberation disintegrates the gel precursor, which nanoparticles size mainly depends on the reaction velocity. Polymerization complex methods are also used, being among them the liquid method which results similar to

that of gel-combustion with citric acid as fuel. Amorphous citrates are formed but, it is necessary in this case, to add ethylenglycol to the nitrates and citrates mixture. This causes a polymerization process enabling to get an homogeneous gel and due to the resulting polymeric network, it is possible to avoid the segregation precipitation or the evaporation of some cations of interest.

- Abrasion and milling (*mechanical processes*) are the oldest techniques [24]. They are based on the milling of coarse powders to obtain very fine particles (balls and planetary-rotation milling). These techniques enable to mill metals or inorganic materials, being obviously not useful for organic materials.

- Processes *via humid chemistry* include the colloidal chemistry, the hydrothermal methods, sol-gel and other precipitation techniques [24]. They consist in mixing solutions of different ions in adequate proportions controlling some parameters like solubility and temperature to precipitate insoluble compounds, which are filtered and dried to produce a powder (the process is completed getting fine powders by milling). The sol-gel technique is particularly investigated because it enables to prepare very fine powders with a low agglomerating degree though, it is usually necessary to start from expensive raw materials and its application results difficult compared with other humid via techniques. It is based on the hydrolysis of an alcoholic solution of a metal alcoxyde which oxyde has to be prepared, resulting a gel by concentration of the hydrolized solution. The gel is finally dried and calcined [25, 26].

- The *in-situ synthesis methods* [24] include the lithography, the physical or chemical deposition from a vapor phase and the spray coating [27]. The particles are obtained by the deposits scraping. These methods are not frequently used for nanocompounds production since they are not too efficient due to the inhomogeneous particles size.

The few considered methods refer to the synthesis of nanopowders but, to get nanomaterials with special forms: nanospheres, nanotubes, nanorods, nanowires, nanobelts, etc., there are a lot of techniques to get them according to their specific applications. Some of these techniques will be mentioned in other paragraphs of this article.

2.2. *Characterization Techniques for Nanostructured Materials*

Among the *physical characterization* measurements the *determination of particle size* of a material is usually the first step in any investigation of a nanocrystalline sample. There are generally three approaches that can be employed: X-ray diffraction (XRD), measurement of the surface by BET gas adsorption and electron microscopy. XRD is a very important experimental technique that has long been used to determine the crystal structure of solids, including lattice constants and geometry, identification of unknown materials, orientation of single crystals, preferred orientation of polycrystals, defects, stresses, etc. *Diffraction peaks positions are accurately measured with XRD,* which makes it the best method to characterize homogeneous and inhomogeneous strains [28]. In nanomaterials, the *peak broadening* as the particle size decreases is a well known phenomenon [29] and can be used to determine the particle size, s, by the Scherrer equation:

$$s = k\lambda / \beta \cos\theta \qquad (1)$$

where k is a constant (usually taken as 0.9), λ is the wavelength of the X-ray beam, β is the full width at half maximum height (FWHM) of a given peak (after removal of the instrumental broadening) and θ is the diffracted angle of the peak. Eq. (1) represents the simplest treatment of peak broadening and it can be extended to include the effect of strain broadening of the peaks [30]. Clearly, this method will only yield an average particle size and will not provide information on the dispersion of the size or the extent of agglomeration of the grains. One of the disadvantages of XRD compared to electron or neutron diffraction is the low intensity of diffracted X-rays, particularly for low-Z materials. It is possible too to use synchrotron radiation diffraction methods, thus avoiding problems related to low intensity of diffracted rays.

SAXS (Small Angle X-ray Scattering) is another powerful tool to characterize nanostructured materials. Strong diffraction peaks result from constructive X-rays interference scattered from ordered arrays of atoms. A lot of information can be obtained from the angular distribution of scattered intensity at low angles. Fluctuations in the electron density or in composition (or both) not necessarily periodic, over lengths of about 10nm or larger can be sufficient to produce appreciable scattered X-ray intensities at angles is $2\theta < 5°$ [31]. The amount and angular distribution of scattered intensity provides information, such as the size of very small particles or their surface area per unit volume, regardless of weather the sample or particles are crystalline or amorphous.

Gas absorption measurements are usually performed with nitrogen or an inert gas and cooling the sample (-196 °C). The surface area, A,

is determined using the classical Brunauer-Emmett-Teller (BET) approach [32]. The particle size, s_{BET}, from these measurements is given by [33]:

$$s_{BET} = 6 / \rho A \quad (2)$$

where: ρ is the density. The factor 6 applies for spherical and cubic particles.

Transmission electron microscopy (TEM), particularly the high resolution HRTEM, is essentially the ideal method of determining the particle size, however, sample preparation can present difficulties. Provided a large number of grains in the sample are observed, the size dispersion and degree of agglomeration can be measured. The high magnification or resolution of TEM is a result of the small effective electron wavelengths, λ, which is given by the de Broglie relationship:

$$\lambda = h / \sqrt{2mqV} \quad (3)$$

where: m and q are the electron mass and charge, h is the Planck´s constant and V is the potential difference through which electrons are accelerated in the microscope (Fig. 1a and 1b).

The Scanning Electron Microscopy (SEM) is a widely used technique to characterize nanostructured materials. The resolution of a modern SEM approaches a few nanometers and the instruments can operate at magnifications that are easily adjusted from ~10 to 300,000x. Not only does the SEM produce topographical information but chemical composition near the surface by the electron microprobe.

The *determination of microstructure* is the most important knowledge related to the properties of nanocrystalline materials. Simple geometric considerations lead to the conclusion that a large fraction of atoms are in the surface of a nanocrystalline sample but it is important to analyse the nature of the surface in terms of the level of atomic order and the structure of grain boundaries. There are two different types of interfaces (or grain boundaries) which have been assumed in nanomaterials. One extreme is that there is an extensive disorder in the interface (several atoms in width). The interfaces, with a high defects density, could be considered as "gas-like" or "liquid-like" regions. The enhancement of diffusion in nanoestructured materials (that will after be widely discussed in this article) was at first explained accepting such an image of the interface. The alternative view is that the interface is similar to a grain boundary in normal bulk materials. In this case, the interfaces would exhibit the usual behaviour, although they would be presenting unusually large number of defects.

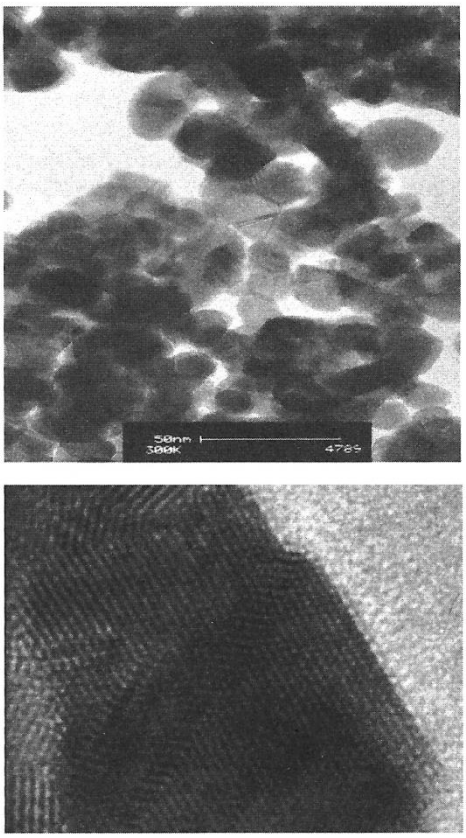

Fig. 1a and 1b. HRTEM images of nanostructured SnO_2 (after [34]).

Unfortunately, HRTEM studies are relatively sparse and other structural techniques have had to be used to investigate the nanostructure, such as: electron diffraction [35], positron annihilation spectroscopy [36] and Extended X-ray Absorption Fine Structure (EXAFS) measurements [37, 38]. EXAFS are the oscillations in the X-ray absorption (a plot of absorption coefficient m versus the incident photon energy) occurring beyond the absorption edge for the emission of a core (K or L shell) electron [39]. The oscillations arise from the emitted photoelectron wave being backscattered and interfering with the outgoing wave. There will be constructive interference if the two waves are in phase (with lower final state energy and a higher probability for absorption) and destructive interference if the waves are out of phase (with higher final state energy and a lower probability for absorption). Thus, as the incident photon energy increases so does the energy of the emitted photoelectron with subsequent changes on its wavelength. Since the distance between the target atom and its neighbours is fixed there will

be shifts in and out of phase and, consequently, the observation of EXAFS oscillations. The oscillations intensity depends on the type and number of neighbours giving rise to the backscattering and an EXAFS Debye-Waller factor (an uncertainty in the distance between target and scattering atoms). EXAFS does not rely on long-range order and is sensitive to the local environment of the target atom out of 5 Å. The Fourier transform of the EXAFS yields a partial radial distribution function in real space with peak areas proportional to average coordination numbers and the Debye-Waller factors. For nanocrystalline samples, the EXAFS signal could be attenuated for two reasons: I) the particle is so small that the average coordination numbers for the neighbouring shells is reduced or II) there is sufficient disorder in the sample (for ex., at the interfaces) so that the Debye-Waller factors are increased. For I) to be operative the particle size has to be very small, typically < 5nm. *Chemical characterization* techniques are the spectroscopies which are usually employed for microcrystalline as well as for nanocrystalline materials and they will be only mentioned in this article. The optical spectroscopy is commonly categorized into two groups: absorption/emission spectroscopy and vibrational spectroscopy. The former determines the electronic structures of atoms, ions, molecules or crystals through the exciting of electrons from the ground to excited states (absorption) and relaxing from the excited to ground states (emission). Optical spectroscopy includes absorption and photoluminescence (PL) techniques. Vibrational spectroscopy provides the information of chemical bonds in the detecting samples and it includes Infrared and Raman spectroscopies. Electron spectroscopy includes the methodology of Energy Dispersive X-Ray Spectroscopy (EDS), Auger Electron Spectroscopy (AES) and X-Ray Photoelectron Spectroscopy (XPS) and the Ionic Spectrometry considers the Rutherford Backscattering Spectrometry (RBS) and the Secondary Ion Mass Spectrometry (SIMS).

3. Research on nanostructured materials at CINSO

3.1. *Synthesis Results of Nanostructured Materials*

In the first PhD thesis on nanocrystalline materials performed in our country in the nineties [22] the study of phenomena produced at the triple interface [nanocrystalline SnO_2/ nanocrystalline ion-conducting oxide/gas] was performed. In the **Applications** Item of this article, it will be described the gas sensor (detecting ppm of CO) resulting from this research. The study considered the phenomena produced at the [Y-TZP/SnO_2] interface in contact with a reducing gas (CO), being the *Y-TZP: Yttria-stabilized Tetragonal Zirconia Polycrystal* with ZrO_2-2.8 mol% Y_2O_3 composition, operating at lower temperatures in comparison with the cubic *FSZ (Fully Stabilized Zirconia)* stable at 800-1200 °C. The retention of this metastable tetragonal phase was possible because it was a nanocrystalline material as it will be described below. Both materials Y-TZP [17-18, 22-23, 40-44] and SnO_2 [19-21, 34, 45-48] were synthesised by the gel-combustion method.

The gel combustion method is based on the formation of an initial gel by thermal concentration of an aqueous solution of nitrates of the desired cations, followed by a combustion process. The reaction between the nitrate ions and the organic fuel is strongly exothermic. The large volume of gases produced during the combustion disintegrates the precursor gel, being this process followed by calcination, which eliminates the organic residues yielding small crystallites of nanometric size. Parameters to be adjusted are, among others, the initial purity and type of nitrates, the organic fuel type, temperature and duration of combustion, being important to evaluate after the synthesis the crystallites size and homogeneity, their morphology and if impurities were retained during the synthesis process.

The *gel-combustion method* was not only used to obtain Y-TZT or SnO_2 but to prepare a novel calcia-stabilized TZP nanoceramics [49], to obtain ZrO_2-Al_2O_3 [50] or CeO_2-Y_2O_3 [51], to synthesize compositionally homogeneous nanocrystalline ZrO_2-35 mol% CeO_2 powders [52] or ZrO_2-15 mol% CeO_2 nanopowders by a pH-controlled nitrate-glycine process [53]. A study of nanocrystalline $Zr_{0.85}Ce_{0.15}O_2$ nanopowders comparing materials synthesized by this method and by spray-pyrolysis, was also performed in [54]. Gel-combustion method enabled to obtain the electrolyte ZrO_2-Y_2O_3 using stoichiometric routes with different aminoacids as fuels [55, 56]. Recently, ZrO_2-Sc_2O_3 nanopowders were synthesized by gel-combustion to be proved as solid electrolyte for fuel cells [57].

Nanostructured ZnO is a very interesting material because it exhibits semiconductive, piezoelectric and pyroelectric properties [58] generating a wide variety of industrial applications (varistors, transparent conductors, UV protective films, gas sensors, etc.). Recently, a project was proposed at CINSO to study the variation of the optical properties of based on ZnO nanomaterials. *Pure ZnO and Al-doped ZnO were synthesized by*

the transference of sols containing the desired nanoparticles by the dip-coating method. In order to study the variation of films properties different ZnO precursor solutions were prepared from solutions of di-hydrated zinc-acetate in absolute alcohol, adding in some cases lactic acid to promote the zinc-acetate hydrolysis and diethanolamine and acetylacetone to improve the films homogeneity [59]. ZnO has applications as material of optical emitting devices in a wide wavelength range and its doping with lanthanides causes the improvement of luminescent properties in comparison with transition elements (Al, for ex.) doped materials. This is due to the fact that transitions inside the 4f levels generate very thin and intensive emission lines which can be selected in the whole range of interest: blue (Tm^{3+}, Ce^{3+}), green (Er^{3+}, Tb^{3+}), red (Eu^{3+}, Pr^{3+}, Sm^{3+}) and the near infrared (Nd^{3+}, Er^{3+}). Recently, the *systematic study of rare earths doping in ZnO was proposed synthesising the nanocrystalline material by gel-combustion methods* [60].

With regards to *special synthesis methods for functional nanomaterials with a determined morphology*, we shall refer to cobaltite *nanotubes* obtained at CINSO to be used for high performance cathodes for IT-SOFCs (Solid Oxide Fuel Cells operated at Intermediate Temperature) [61, 62]. A new type of highly porous nanostructured cathodes exhibiting very low polarization resistance, prepared from $La_{0.6}Sr_{0.4}CoO_3$ nanotubes following a very simple procedure, is presented here and SOFCs performance will be described in the **Applications** paragraph of this article.

Tubular structures formed by assembling manganite nanoparticles have already been successfully synthesized by Leyva et al. [63, 64] presenting these structures a very high specific area and having recently been suggested as cathodes for SOFCs [65]. However, manganites are not good candidates for IT-SOFC because they are poor ionic conductors in the intermediate temperature range [66]. In this case, it is better to choose cobaltites for this type of SOFCs. The chosen material to obtain nanotubes was the $La_{0.6}Sr_{0.4}CoO_3$ (LSCO) compound since it is nowadays one of the most used cathodes in IT-SOFCs due to its significant mixed ionic-electronic conductivity in this temperature range [66]. In case of LSCO nanotubes, they were synthesized using the pore wetting technique to obtain tubular structures. Commercial polycarbonate membranes with pore size of 800 nm were used as template and filled with a nitrate precursor solution. The membranes were further treated under microwave radiation for a few minutes and

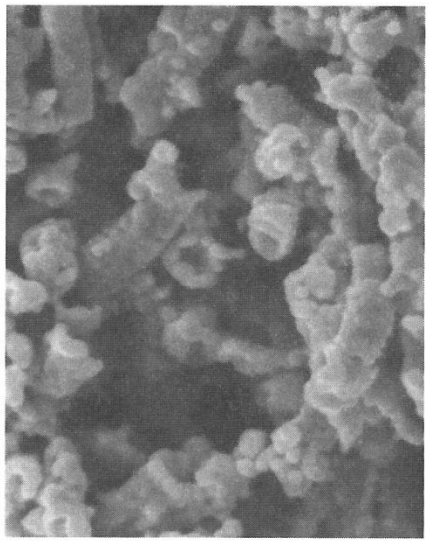

Fig. 2. SEM micrograph of LSCO nanotubes (after [62]).

then calcined for 10 min at 750-900 °C, obtaining the perovskite desired structure, as confirmed by X-ray diffraction. Nanotubes sintered at 800 °C (Figure 2) exhibited a crystallite size of about 20 nm and BET specific surface area of 43 m^2/g, showing that nanotubes are formed by disagglomerated crystallites. The high specific surface area resulted useful to prepare a high-performance cathode.

Another *special synthesis method to obtain nanomaterials* was used for the preparation of Ni catalyzers to produce the catalytic oxidation of methane in anodes of one-chamber IT-SOFCs [67]. CeO_2 and CeO_2-ZrO_2 were chosen by their convenient structural and electronic properties. Besides, ceria exhibits the capacity for oxygen storage because of cerium cation possibility to easily change between their reducing and oxidizing states (Ce^{3+}/Ce^{4+}). Ceria and zirconia oxide, with a nominal composition: $Ce_{0.9}Zr_{0.1}O_2$, was synthesized by gel-combustion method using glycine as fuel [68] to obtain a nanometric particle size. Solids were impregnated with a Ni solution so as to obtain two nominal contents of Ni: 9% and 50% (m/m).

3.2. *Characterization Results of Nanostructured Materials*

Previously it was mentioned that several ionic nanomaterials: ZrO_2-Y_2O_3 (cubic and tetragonal phases), CaO-TZP, ZrO_2-CeO_2 solutions, ZrO_2-Sc_2O_3 and the nanosemiconductive SnO_2 were synthesized at CINSO [17-23, 40-57]. In all these cases, the usual characterization techniques

included: conventional XRD to identify the obtained compounds, measurement of the mean crystallite size by the broadening of XRD diffraction peaks (Scherrer technique), refining of crystallographic parameters by the Rietveld method evaluation of BET specific area and observation techniques to study the morphology of crystallites (like: ESEM-Environmental Scanning Electron Microscopy, TEM, HRTEM or SEM). In case of electrical characterization of ionic materials to be used as electrolytes of fuel cells, EIS measurements were required. With regards to the characterization of pure and doped ZnO for optical measurements, in case of pure ZnO and Al-doped ZnO [59] nanomaterials were characterized with conventional XRD, grazing incidence XDR (to observe the nanostructures formation), reflectivity (XRR) and grazing incidence low angle diffusion (GISAXS) techniques with synchrotron radiation. It was possible to determine a mean thickness of films by XRR. The films density decreases with doping. No relation between the layers quantity and the thickness was found, thus probably indicating that successive coatings wash the previous deposited material. In case of lanthanides-doped ZnO, only conventional XRD was used to identify the materials and Scherrer technique to measure the crystallite mean size [60].

In the reference [69] the first synthesis and characterization of nanomaterials obtained at CINSO were reviewed. In this section, we shall refer to papers in which different techniques of characterization were reported applied to functional nanomaterials usually synthesized by the gel-combustion method.

Nanostructured ZrO_2-Y_2O_3, ZrO_2-CeO_2 or ZrO_2-CaO systems were intensively studied and different techniques were applied to characterize them: for ex. compositionally homogeneous nanocrystalline yttria-, ceria- or CaO-doped zirconia powders mainly studied by conventional XRD [70-73] or XRD with synchrotron radiation [74-76]; the metastable t"-form of the tetragonal phase ZrO_2-10mol% Y_2O_3 powders using the Hyperfine characterization - Perturbed Angular Correlations technique (we shall refer again to the results of this work upon considering the tetragonal phases of these system) [77]; the distribution of grain size in nanocrystalline systems by TEM [78]. Also absorption techniques with synchrotron radiation were applied to characterize the above mentioned nanocrystalline systems, for ex. the EXAFS technique to determine: the local structure of the metal-oxygen bond in compositionally homogeneous nanocrystalline ZrO_2-CeO_2 solid solutions [79] being the characterization completed with Raman spectra analysis; the crystal structure of nanocrystalline compositionally homogeneous ZrO_2-Y_2O_3, ZrO_2-CeO_2 or ZrO_2-CaO powders or the study of the nanostructured solid solutions of the two former systems [80-83]; the local structure of the tetragonal phase in nanostructured ZrO_2-based materials" [84]; the structure of nanoporous zirconia based powders synthesized by different gel-combustion routes [85] and more generally the crystalline structure and local order in based on zirconia nanos-tructured materials [86]. The nanoporous structure of the zirconia based powders was studied in [87].

LSCO nanotubes [63, 64] for IT-SOFCs, were characterized by conventional XRD, proving that the desired perovskite structure was obtained. The application of Scherrer technique enabled to evaluate the crystallite size: 20nm and BET technique the specific area: 43 m^2/g, showing that nanotubes are formed by disagglomerated crystallites. The high specific surface area is expected to be very useful to prepare high performance cathodes. CeO_2-10 mol% Sm_2O_3 (SDC) electrolytes pellets were painted with an ink made with LSCO nanotubes calcined at 800ºC and commercial Nextech Ink Vehicle (NIV). Known processes to attach the electrodes on the electrolyte involve temperatures ~ 1000 °C and times of ~ 1 or 2 hours with slow heating and cooling rates, being this option improper for the preparation of a nanostructured cathode. An original method was then developed attaching the cathodes by heating the sample at 1000-1200 °C with very fast heating and cooling rates (around 200 °C/min) and dwell times of 1-10 min. In addition, this method allowed us to obtain a cathode in only several minutes. Electrical behavior of cathodes was studied with EIS.

$Ce_{0.9}Zr_{0.1}O_2$ was used as supporting nanomaterial for Ni-catalyzers employed as anodes of IT-SOFCs [67]. The template was synthesized by gel-combustion [68] and characterized by BET (specific area and total volume of pores). Analysis to determine the carbon content in the fresh specimen was performed by the complete and instantaneous oxidation of specimen by a flash combustion identifying the combustion gases by chromatography. Conventional XRD was used to characterize the templates, being these supporting materials tested by Temperature Programmed Reduction-TPR in an usual laboratory equipment. The quantity of consumed H_2 (reducing agent) was determined from the signal of a thermal conductivity detector (TCD) thermostated in an oil bath. The catalytic functioning of these anodes will be considered in the **Application** paragraph referred to IT-SOFCs performance.

3.3. *Metastable Phases Retention in Nanostructured Materials*

It was already mentioned that zirconia-based ceramics are widely used because of their electrical and mechanical properties, exhibiting for ex. a high ionic conductivity at high and intermediate temperatures (as it will be considered in the next paragraph of this article) allowing their use in solid oxide fuel cells (conventional HT- SOFCs and IT- SOFCS), oxygen sensors, oxygen pumps, etc. [88, 69]. On the other hand, they are though, wear resistant and they show a low heat conductivity, so these materials are also useful as structural ceramics [89, 90]. Besides, if zirconia-based ceramics are nanostructured, new or improved properties were found: the retention of unstable phases, enhanced ionic conductivity, superplasticity, among others, being some of them intensively studied at CINSO [17-22, 40-57, 61-62, 67-87] and used for new applications: solid electrolytes [91,92], electrode materials [61, 62] and catalysts [67, 93] for intermediate temperature fuel cells IT-SOFCs or improved gas sensors [19-21, 34, 45-48]. It is interesting to point out that the conventional HT-SOFCs operate at high temperature (800-1200°C) using as solid electrolyte: the HT cubic phase of ZrO_2-Y_2O (with high yttria concentrations: 8-10 mol%) and conduction is produced by oxygen vacancies (O^{2-}). The retention of metastable tetragonal phases (good O^{2-} conductors too) enabled to decrease the operation temperature of fuel cells (IT-SOFCs) to an intermediate temperature working range of 550-750 °C saving energy, increasing the mean life of cell materials, avoiding the use of noble materials and, consequently, decreasing their cost.

3.3.1. Pure ZrO_2

At the atmospheric pressure, pure zirconia exhibits three polymorphs of monoclinic ($P2_1/c$ space group) [94, 95], tetragonal ($P4_2/nmc$) [96] and cubic ($Fm\bar{3}m$) [97] symmetries. The monoclinic phase (m) is stable at room temperature and transforms to the tetragonal phase (t) at 1170 °C during heating. At 2370 °C, the t-phase transforms to the cubic one (c). Both transformations are martensitic in nature and reversible on cooling and the t → m transformation occurs at a lower temperature (about 950 °C). The tetragonal structure is derived from the fluorite type structure of the cubic phase by elongating one of the three equal crystallographic axes of the cubic structure and displacing the oxygen ions from their ideal positions in this phase along the same axis. For high pressures, an orthorhombic phase has been found [98].

The high temperature tetragonal and cubic phases can be retained at lower temperatures (even at T_{room}) by doping with metal oxides (MO or M_2O_3) forming solid solutions with zirconia. The doping cations with a lower valence state, replace the Zr^{4+} creating vacancies in the oxygen sublattice (major carriers for conduction at higher temperature). The compositional range for the stabilisation of the tetragonal and/or cubic phases is narrow and depends on temperature and doping, being Y_2O_3, CaO, MgO some usual stabilizers.

CeO_2 is also used but, in this case, the valence state of the doping cation is usually the same that for Zr (+4) creating controversies in the stabilisation mechanisms of the t and c phases [89]. A large change of volume (3-5%) occurs during this transformation, which can lead to the disintegration of a ceramic body during cooling from the sintering temperature but, the "transformation toughening mechanism" is produced [90] avoiding the fracture of material.

For high temperatures, zirconia-based binary systems usually present three regions according to their composition. For low doping concentrations, the tetragonal phase can be stabilized; at intermediate concentrations a mixture of tetragonal and cubic phases is retained [90, 99]. At T_{room}, the stable phase is the monoclinic one but, under certain conditions, the tetragonal phase can be retained. Zirconia-based ceramics can be classified into three groups according to present phases [90, 99]: TZP (Tetragonal Zirconia Polycrystal) with tetragonal phase, PSZ (Partially Stabilised Zirconia) with a mixture of tetragonal and cubic phases and FSZ (Fully Stabilised Zirconia) with cubic phase.

In spite that the t-phase is not stable at room temperature, it was found that this structure can be retained in case of ceramics exhibiting a mean grain size lower than a critical value. For ex., in case of ZrO_2–Y_2O_3 ceramics, this critical size varies from 0.2 to 1mm for 3 mol% Y_2O_3 compositions [100]. Considering the required small grain size to retain the t-phase, it is convenient to prepare ceramics starting from zirconia-nanocrystalline powders, which are synthesized by numerous different methods, among them: co-precipitation [101-103], amorphous citrate process [103], sol-gel [104-106], polymerised complex method [102, 107-109] or gel-combustion [18, 20, 49, 53, 110-114].

Although, it is believed that the surface free energy has an important role for stabilisation [90], *stresses and defects cannot be disregarded* [115].

Most of these studies are based on the relation between the crystallite size and microstrains as studied by X-ray line profile analysis [116].

Conditions to retain the t-phase in case of ceramic powders is not clearly understood yet, but it was accepted that a crystallite mean size between 10 to 20nm was required to stabilize t-phase of pure (undoped) zirconia nanopowders. However, in recent works at CINSO [117, 118] the crystal structure of these nanopowders was reported. Nanopowders were synthesized by different wet chemical routes, using synchrotron X-ray diffraction demonstrating that: I) pure zirconia nanopowders with average crystallite sizes ranging from 5 to 10nm exhibited the t-phase and II) that a t → c transition for decreasing crystallite could eventually occur at a very small critical crystallite size.

Phases of pure zirconia are:

- ***Monoclinic phase (m-phase):*** Yardley [119] determined the space group $P2_1/c$, formed by four ZrO_2 molecules per unit cell (resulting from a distorsion of fluorite structure) being the structure of m-phase evaluated in [120, 121]. Figures 3a, 3b and 3c report the three zirconia polymorphs. Figure 4 shows the Zr coordination polyhedron in m-phase. Zr^{4+}ions have seven-fold coordination with oxygen forming a tetrahedron and being the four O_{II} nearly on a plain and with triangular coordination with three O_I which are nearly on a plain parallel to that formed by the O_{II}.

- ***Tetragonal phase (t-phase):*** Teufer [122] determined that the t-phase belongs to the $P4_2/nmc$ space group and that it exhibits the slightly distorted fluorite type structure, which is described as a non primitive face-centered t-phase or as 'pseudo-fluorite' with a unit cell twice the volume of the primitive cell, Figure 5. In t-phase, each Zr is surrounded by 8 oxygen ions, four at a distance of 2.065 Å (thin tetrahedron) and four at 2.455Å (larger tetrahedron rotated 90° to the former) Figure 6.

- ***Cubic phase (c-phase):*** It has the pure fluorite type structure and corresponds to the Fmm space group and has a lattice parameter: 5.080Å being this value similar to $a_f = \sqrt{2}a_t$ and $c_f = c_t$ parameters of the t-phase. In consequence, it is very difficult to quantitatively differentiate between the two phases by X-ray or electron dif-

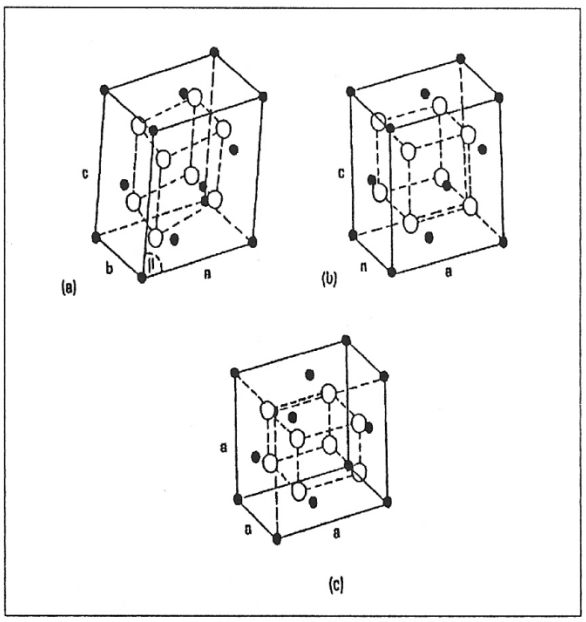

Figs. 3a, 3b and 3c. Schematic representation of the three zirconia polymorphs: a) monoclinic, b) tetragonal and c) cubic. Only cubic has fluorite-type structure, the other two exhibit the pseudo-fluorite type structure.

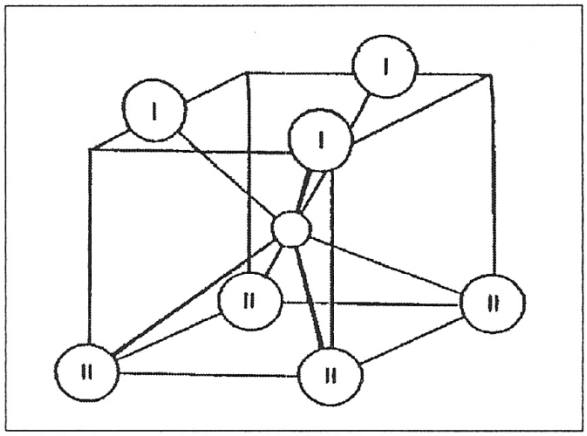

Fig. 4. Zr^{4+} ions coordination polyhedron in m-phase. O_I and O_{II} : oxygen in different positions.

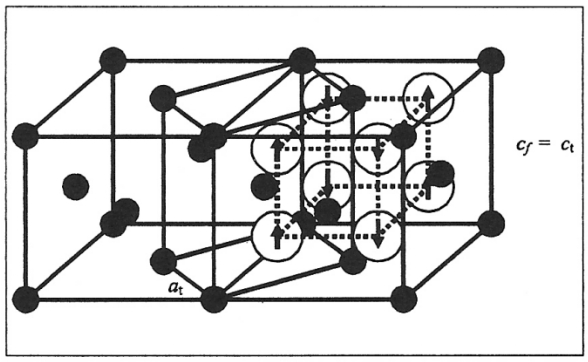

Fig. 5. Crystal structure of t-phase showing the relationship between the 'pseudo-fluorite' and the primitive t-cell. Solid circles: Zr^{4+} and dopant cations, open circles: O^{2-} anions. Arrows: displacement of O^{2-} anions along the c-axis.

fraction when both polymorphs are present. But, the separation of peaks corresponding to both c- and t-phase was possible by higher energy X-ray diffraction (Synchrotron Light) [117, 118] and results of these works were compared with those of [123, 124]. Materials synthesized at CINSO by different routes of gel-combustion method, always exhibited the tetragonal phase at room temperature [117, 118] in contrast with results of above mentioned works [123, 124] which reported the retention of the cubic phase at room temperature from conventional XRD measurements. Other XRD studies reported in the literature on pure ZrO_2 nanopowders synthesized by other methods [125-128] also informed the retention of the cubic phase at room temperature. However, results at CINSO [117-118] suggest that the retained phase in these materials - with crystalline sizes ranging from 5 to 10 nm - is the tetragonal one. This contradiction of previous works can be explained by the higher quality of synchrotron XRD data that made possible the detection of small Bragg peak splittings and very weak Bragg reflections that cannot usually be detected using conventional XRD, Figures 7a, 7b and 7c. Though monoclinic is the stable polymorph of pure ZrO_2 at room temperature, it could be clearly demonstrated that, in nanopowders (5-10 nm), the tetragonal phase is retained at room temperature and only traces of the monoclinic phase may eventually be present. In spite of the fact that the XRD studies has demonstrated the retention of the tetragonal phase, these results show that both, the axial ratio and the displacement of the O^{2-} anions from their positions in the cubic phase decrease with decreasing crystallite size, suggesting the existence of the tetragonal-to-cubic transition with a very small critical crystallite size.

3.3.2. Doped zirconia: ZrO_2-Y_2O_3, ZrO_2-MgO, ZrO_2-CaO and ZrO_2-CeO_2 systems

In spite of being published in a previous authors' review [69] the equilibrium phase diagrams of the three systems are included to clarify

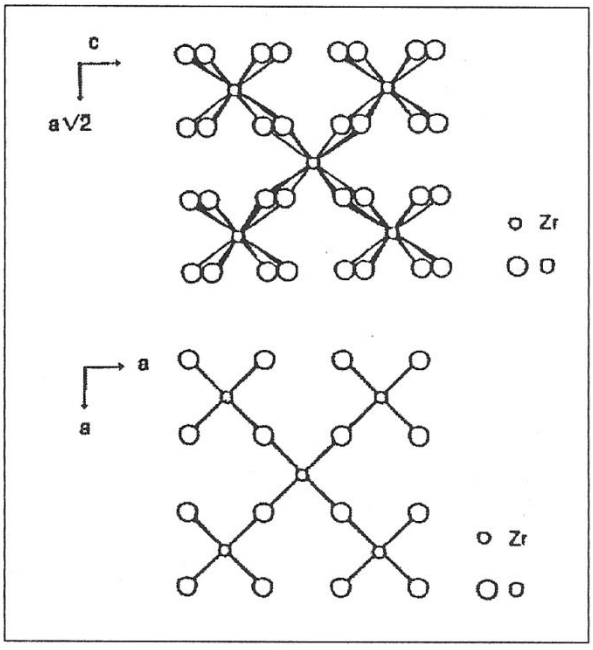

Fig. 6. Schemes showing the octahedral coordination of Zr^{4+} ions in tetragonal zirconia (a), projection along (110) and in cubic zirconia (b), projection along (100) [121].

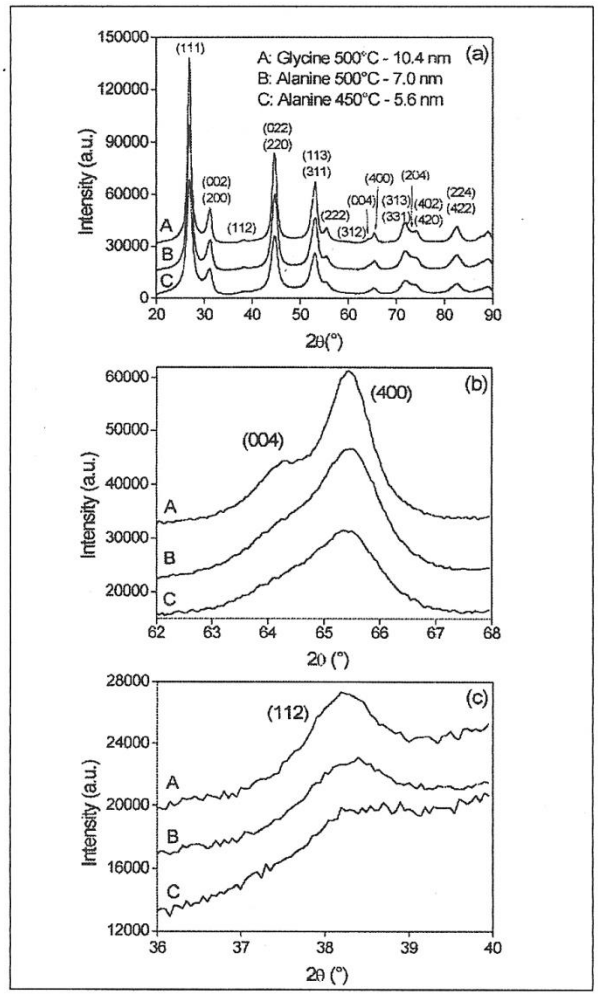

Figs. 7a, 7b and 7c. a) XRD patterns of pure ZrO_2 (synthesized by different routes of gel-combustion method), counting time:2s/step, all the peaks have been indexed using a tetragonal cell, b) Detail of the splitting of the (400) and (004) reflections, counting time: 12s/step and c) Detail of the (112) reflection, counting time: 12s/step.

the present phases. The ZrO_2-Y_2O_3 equilibrium phase diagram by H. G. Scott [129], Figure 8 is analyzed and it is pointed out that it is the most accepted diagram since it agrees with all the reported experimental data. It shows wide t and (t + c) fields, which allow the TZP and PSZ synthesis. If the grain size is small enough, the t-phase can be stabilized by the low eutectoid temperature and the high solubility limit predicted by the equilibrium phase diagram [89]. As it was above reported, for compositions from 2 to 3mol% Y_2O_3 [87], the critical grain size to retain the t-phase was between 0.2 to 1 μm. For rapid cooling from high temperatures, a new t-phase (t´) with different characteristics of the usual one was found. The 'tetragonality' or axial rate:

$(c/a)_f$ = 1.003-5 is lower that of the t-phase $(c/a)_f$ = 1.010-15 with an yttria content similar to that of c-phase. The t-phase is resistant to transform to m-phase but, it is nevertheless metastable transforming to t and c-phases.

Researchers at CINSO have found a t"-form in compositionally homogeneous nanocrystalline powders of ZrO_2-12mol%Y_2O_3 t-phase by X-ray diffraction and applying the Rietveld method [130, 131]. These powders exhibited a t-phase, with an axial ratio of unity but with the oxygen ions displaced from their ideal fluorite positions along the c-axis. Previously, Yashima et al. [102, 103, 108] have studied arc melting ZrO_2-Y_2O_3 powders finding that the t'/t" boundary was located at 9mol%Y_2O_3 and the t'/c boundary at 11mol%Y_2O_3. Lamas et al. [130] applied the Rietveld method to XRD data discriminated between t" and c-phases by refining of the fractional z coordinate of oxygen ion in the tetragonal asymmetric unit. Comparing results of [130] with Yashima's data [102, 103, 108] Lamas et al. have found that nanocrystalline powders present a larger oxygen displacement in comparison with arc-melted material. This displacement decreases with increasing calcination temperature depending, consequently, the composition range of the t"-region of the crystallite size, which result larger for nanocrystalline materials.

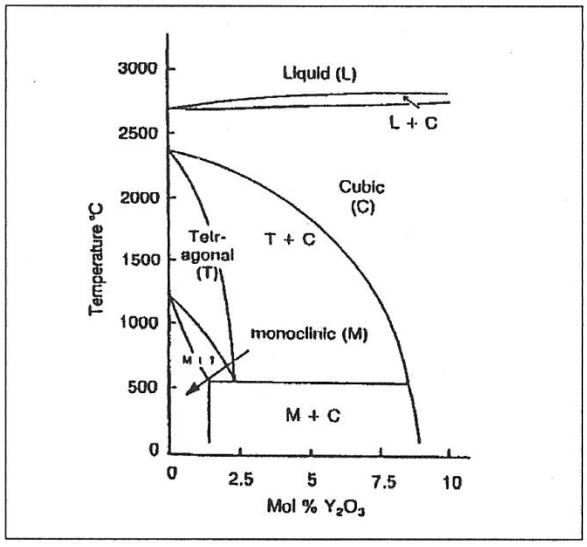

Fig. 8. Equilibrium phase diagram of ZrO_2-Y_2O_3 system by H. G. Scott [129].

If the metastable t"-form of nanocrystalline t-phase ZrO_2-10mol%Y_2O_3 powders is characterized by Perturbation Angular Correlations (PAC) technique [77], the evaluated hyperfine interaction allows a clear distinction between the Zr surroundings in the t"-form and those corresponding to the other forms of the t-phase. Oxygen vacancies are moved by diffusion involving a very low activation energy. As the powders are heated, a transformation occurs at ~ 560 °C consistent with a t"→ c-transition, as evaluated by DSC technique suggesting a transformation of a higher order than the first one. Nanostructured solid solutions of ZrO_2-Y_2O_3 were analysed by EXAFS technique at the LNLS, SP, Brazil [73, 132] in order to determine the neighbours (O^{2-}) of the Zr^{4+} ions in both, cubic and tetragonal phases. This technique enables to acquire information of near-neighbour distance distributions, coordination numbers and, less directly, bond angles. EXAFS proves only the first few coordination shells and, therefore, it does not reveal nanometer-scale structure, however EXAFS contains crucial chemical-specific local structural information but together with simultaneous quantitative diffraction it still exhibits the highest importance [87].

The equilibrium phase diagram of ZrO_2-MgO system was proposed by Grain [133], Figure 9. It shows nearly no solubility in m-zirconia up to 900 °C, appearing some solubility at higher temperatures: maximal value 1.6mol% MgO at 1120 °C and dropping to zero at 1190 °C. On the opposite, a higher solubility is found in t-zirconia with a maximal value of 1.7mol% MgO at 1400 °C. The solubility of MgO in c-zirconia is higher and by this, PSZ and FSZ ceramics are obtained while TZP ceramics have not been obtained at room temperature. The preparation of Mg-PSZ ceramics requires thermal treatments at high temperature (~ 1800 °C depending on composition) followed by a fast cooling. This procedure retains the c-phase but very fine t- particles precipitate by cooling.

The most frequently reported equilibrium phase diagram of ZrO_2-CaO system is the one proposed by Stubican et al. [134]. In this system as in ZrO_2-MgO, Figure 10, the presence of large (t+c) and c-regions allows the PSZ and FSZ ceramics preparation but, in ZrO_2-CaO phase diagram, the t-field is wider than that of the former and Ca-TZP could also be obtained by Lamas et al. [49] for the first time. These materials present a very small critical grain size to retain the t-phase (~ 150 nm for a ZrO_2-4mol%CaO) being necessary to use a fast-firing treatment of samples at high temperatures (1400-1500°C) which allows densification of materials avoiding however a significant grain growth. In case of Ca-PSZ ceramics, a similar procedure to that described for Mg-PSZ, is used to prepare them from the mixture of raw oxides. However, fine-grained and dense Ca-PSZ ceramics could be prepared by a fast-firing treatment applied to compacted pellets obtained from nanocrystalline powders [134].

The equilibrium phase diagram of the ZrO_2 - CeO_2 system was proposed by P. Durán et al. [135], Figure 11. This system exhibits a wide tetragonal region allowing the preparation of Ce-TZP ceramics with CeO_2 contents ranging from 12 to 18 mol%, showing a wider compositional range than in case of Y-TZP compounds. At first, powders were produced with large grain sizes (a few microns). On 2000 and 2001, the t-phase of ZrO_2 – 2-15mol%CeO_2 [136, 137] with an average crystallite size of 8-14 nm was synthesized by nitrate-glycine gel-combustion and found phases were studied with X-ray diffraction and Raman Spectroscopy. Fully tetragonal materials were obtained for a CeO_2 contain of 5mol% or higher maintaining a very low crystallite mean size. At the same time, compositionally homogeneous, nanocrystalline ZrO_2-35mol% CeO_2 was synthesized at CINSO by gel combustion [52] exhibiting the t'-form of the tetragonal phase. The X-ray

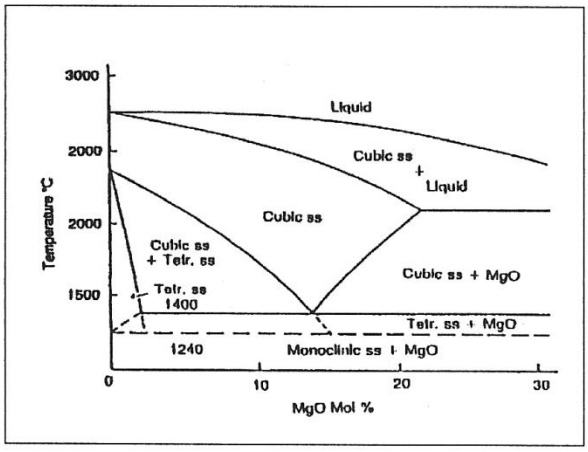

Fig. 9. Equilibrium phase diagram of ZrO_2-MgO system by C. F. Grain [133].

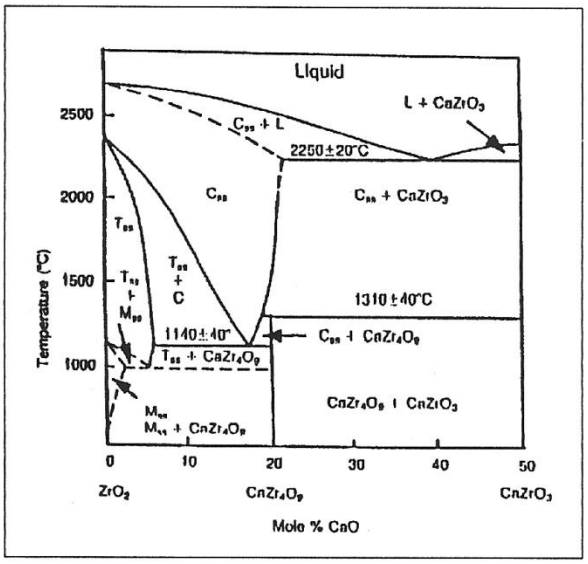

Fig. 10. Equilibrium phase diagram of ZrO_2-CaO system by V. S. Stubican et al. [134].

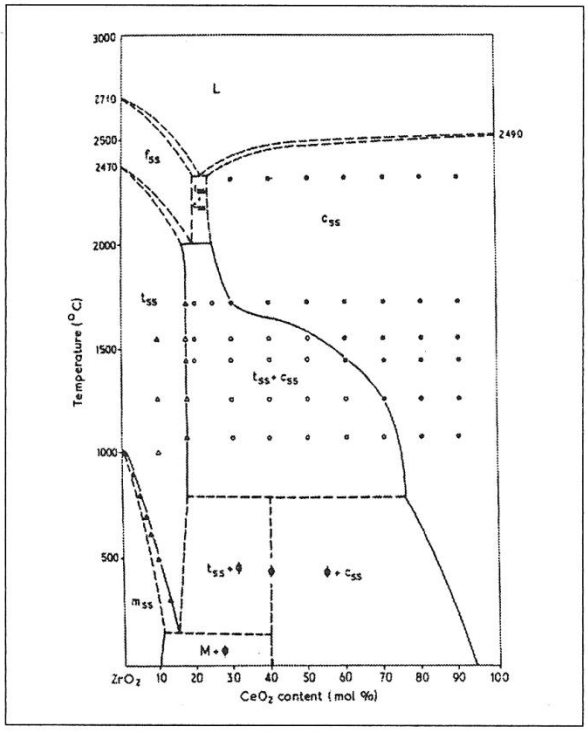

Fig. 11. Equilibrium phase diagram for ZrO_2-CeO_2 by P. Durán et al. [135].

diffractogram of calcined at 600 °C powders exhibited the t-phase by the splitting of the $(400)_t$ and $(004)_t$ reflections, Figure 12. The splitting is characteristic of the t or t´-forms since the t"-form and the c-phase only presents one reflection. Since these powders composition is larger than the solubility limit predicted by the equilibrium phase diagram [135], powders calcined at 600 °C exhibited the t'-form of the t-phase. Crystallite size was ~ 13nm as evaluated X-ray line broadening method.

On 2003, powders of compositionally homogeneous, nanocrystalline ZrO_2 –10, 30, 50, 70 and 90mol% CeO_2 powders have been synthesized and characterized by X-ray diffraction and Raman Spectroscopy [110]. All powders with CeO_2 content up to 70mol% exhibited the t-phase whereas the ZrO_2-90mol% CeO_2 presented the c-phase. The axial ratio c/a decreased with the increasing CeO_2 content and became the unity for ZrO_2-70mol% CeO_2. Analyzing the X-ray diffraction data using the Rietveld method, it was found that this material exhibited the t"-form of the t-phase (the oxygen atoms were displaced from their ideal sites in the c-phase along the c-axis). Raman spectroscopy confirmed X-ray data.

The crystal structure of numerous nanocrystalline ZrO_2-CeO_2 solid solutions (as synthesized by a pH controlled nitrate-glycine gel-combustion process) were studied at CINSO [76]. By the use of synchrotron XRD, small peaks of the t-phase, corresponding to forbidden reflections in case of the 'perfect cubic fluorite structure', were clearly detected. By monitoring the most intense of these reflections, 112, as a function of the CeO_2 content, the tetragonal-cubic phase boundary was found to be at 85mol% CeO_2. For a CeO_2 content up to 68mol%, a tetragonal phase with c/a >1 (known as the t'-form) was detected, whereas, between 68 and 85mol% CeO_2, the existence of a t-phase with c/a = 1 and oxygen anions displaced from their ideal positions in the cubic phase (the t"-form) was also verified. Solid solutions with higher CeO_2 contents exhibit the cubic fluorite-type phase.

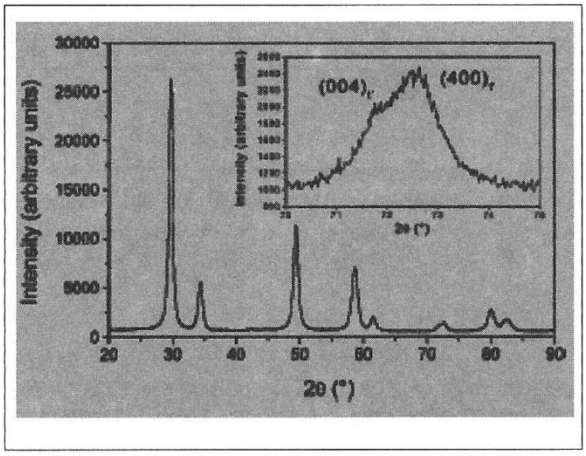

Fig. 12. Diffractogram of the nanocrystalline ZrO_2-35 mol% CeO_2 powders calcined at 600°C. The inset shows the splitting of the $(400)_t$ and $(004)_t$ reflections.

Besides, local structure of metal-oxygen bond in compositionally homogeneous, nanocrystalline zirconia-ceria solid solutions (as synthesized by the same above mentioned gel-combustion technique) [76] were characterized by Raman also by Extended X-ray Absorption Fine Structure (EXAFS) spectroscopies [79]. These techniques revealed once again a tetragonal to cubic phase transition as a function of CeO_2 content, as it was observed in the previous synchrotron X-ray diffraction study [76]. The t/c phase boundary was found at (85 ± 5) mol% CeO_2. The EXAFS study demonstrated that this transition is related to a tetragonal-to-cubic symmetry change of the Zr-O first neighbour coordination sphere, while the Ce-O coordination sphere preserves its cubic symmetry over the whole composition range.

ZrO_2-CeO_2 solid solutions are extensively used as promoters in catalysts which are applied to control the emissions of NO_x, CO and hydrocarbons from automotive exhausts [138]. If pure CeO_2 is compared with ZrO_2-CeO_2 materials, the last exhibit higher thermal stability and oxygen storage capability.

3.4. *Fast Ionic-Transport in Nanostructured Oxide-Ion Solid Electrolytes*

In conventional polycrystalline solid electrolytes, the grain boundaries partially block the ionic transport, causing an extra contribution to the total resistance and, therefore, the total conductivity decreases with decreasing grain size. Then, the total conductivity is limited by the bulk conductivity of the material, which only depends on its crystal structure and composition. In the case of nanostructured solid electrolytes, it is to be expected that the grain boundary diffusion plays an important role, since it is much faster than bulk diffusion [139-141]. Even though this prediction is widely accepted, only a few authors have experimentally confirmed it. For ex., Kosacki and coworkers observed a remarkable enhancement of the total ionic conductivity in nanostructured yttria-stabilized zirconia (YSZ) and CeO_2-Gd_2O_3 thin films, between one or two orders of magnitude, compared to that of microcrystalline ceramics or single-crystals [142, 143].

These authors also found that this phenomenon is related to the reduction of the activation energy for ionic transport, E_a, and attributed this change to the segregation of impurities, mainly Si, to the grain boundaries. Differently, such enhancement of the ionic conductivity of ceria or zirconia-based ceramics has not been observed in other works [144, 145]. Recent reviews pointed out this strong controversy [140, 141, 146].

In a recent paper [91] we reported the enhancement of the total ionic conductivity in nanostructured heavily-doped ceria dense pellets. It was shown that the total ionic conductivity (as measured with EIS) increases in about one order of magnitude in these nanoceramics compared to the intrinsic bulk conductivity of these materials, evaluated in conventional microcrystalline ceramics. Figure 13 a and b show a) the Arrhenius plots of CeO_2-10mol% Y_2O_3 (CYO) and b) CeO_2-10mol% Sm_2O_3 (CSO) ceramics for different grain sizes

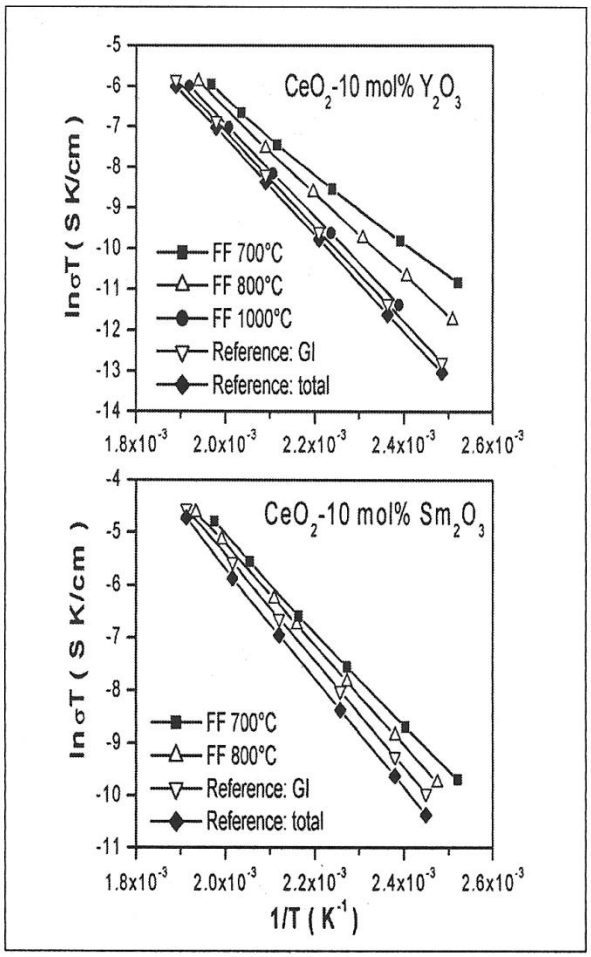

Figs. 13 a and b. Arrhenius plots of a) CeO_2-10mol% Y_2O_3 (CYO) and b) CeO_2-10mol% Sm_2O_3 (CSO) ceramics for different grain sizes.

since the total ionic conductivity has been fitted as a function of temperature (T) following the classical Arrhenius plot:

$$\sigma = (\sigma_0 / T) \exp (- Ea / k_B T) \qquad (4)$$

where: Ea is the activation energy for ionic migration, k_B is the Boltzmann constant and σ_0 is the pre-exponential factor (a constant related to the density of charge carriers which are oxide vacancies in this case). Table I. reports the pre-exponential factor and activation energy for total ionic conductivity for all the studied samples. It was observed that both, Ea and σ_0 decrease with the decreasing average grain size. For the samples with the smallest grain size it has been noted a change in the Ea as a function of the temperature and Table I reports the results found for the two regimes at higher and lower temperatures. In all cases, this change was found at ~ 190 °C. The Ea values at higher temperatures are similar to those Ea values corresponding to the microcrystalline ceramic taken as reference, exhibiting the Ea a sharper change with decreasing grain size. This fact indicates that the lower temperature regime is controlled by grain boundary conduction (with a low activation energy) and at higher temperatures, the volume conduction predominates.

We also showed that the impedance spectra observed for nanoceramics is very different to that generally found for conventional microcrystalline materials, Figure 14 exhibiting only one flat arc instead of the usual two semicircles attributed to bulk and grain boundary conduction processes. This behavior, also observed in other

Table I. Pre-exponential factor and activation energy for total ionic conductivity for all the studied samples

Samples	Pre-exponential factor (K/Ωcm)	Activation energy (eV)
CYO 700 °C; high temp.	$1.4*10^6$	0.88 ± 0.02
CYO 700 °C; low temp.	$2.5*10^4$	0.72 ± 0.02
CYO 800 °C; high temp.	$4.8*10^6$	0.94 ± 0.02
CYO 800 °C; low temp.	$5.8*10^5$	0.86 ± 0.02
CYO 1000 °C	$8.0*10^6$	0.98 ± 0.01
CYO 1300 °C	$1.2*10^7$	1.02 ± 0.01
CYO 1300 °C; grain interior	$1.0*10^7$	1.00 ± 0.01
CYO 1300 °C; grain boundary	$1.9*10^8$	1.08 ± 0.01
CSO 700 °C; high temp.	$1.1*10^6$	0.82 ± 0.02
CSO 700 °C; low temp.	$1.6*10^5$	0.74 ± 0.02
CSO 800 °C	$8.6*10^5$	0.81 ± 0.01
CSO 1300 °C	$5.5*10^6$	0.92 ± 0.01
CSO 1300 °C; grain interior	$2.5*10^6$	0.87 ± 0.01
CSO 1300 °C; grain boundary	$3.6*10^7$	0.96 ± 0.01

phenomena dominated by grain boundaries, strongly suggests the predominance of grain boundary conduction in nanoceramics. As Kosacki et al [142, 143], we have found that E_a is lower for the nanoceramics in comparison with that of microcrystalline materials. Differently to these authors, we proposed that the enhancement of the total ionic conductivity can be accounted for by the raise of the parallel grain boundary conductivity in the nanostructured samples, coupled to an increase of the grain boundary ionic diffusivity with decreasing grain size.

We proposed, then, a physical mechanism behind the remarkable enhancement of the ionic conductivity reported in nanostructured oxide-ion solid electrolytes. Interestingly, the behavior of these nanoceramics at low temperatures resembles that of other families of solid electrolytes (materials with delocalized carriers), which are expected to have a different conduction mechanism. In the present case, the delocalized carriers in the nanoceramics have been identified as free oxygen vacancies located at the grain boundaries, which dominate the ionic transport due to the high volume fraction of the grain boundaries.

The transport properties of heavily-doped CeO_2-based nanoceramics were studied by electrochemical impedance spectroscopy (EIS) measurements in air for temperatures ranging from 125 to 250 °C. In our previous work [91] it has been demonstrated that the electronic conductivity is negligible in this temperature range for all the studied samples and, therefore, the conductivity determined by EIS measurements is only due to ionic transport. CeO_2-10 mol% Y_2O_3 (CYO) and CeO_2-10 mol% Sm_2O_3 (CSO) dense

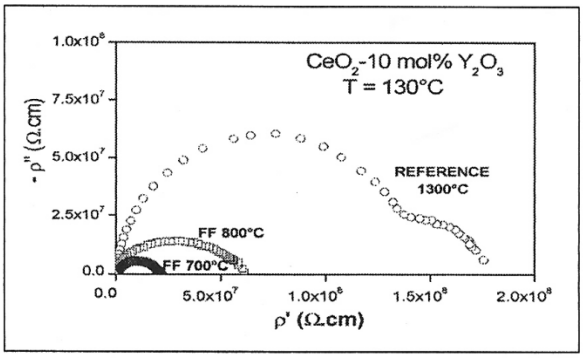

Fig. 14. EIS spectra of nanostructured CeO_2-10mol% Y_2O_3 ceramics (fast firing at 700°C), measured in air at 130°C. The spectrum of microcrystalline CeO_2-10mol% Y_2O_3 (reference) prepared by conventional sintering at 1300°C is given for comparison.

nanoceramics with average grain sizes in the range of 25-50 nm were prepared from high-specific surface area nanopowders by a fast-firing process. The relative density was higher than 92% in all the samples. Microcrystalline specimens, prepared by conventional sintering at high temperatures, were also studied for purpose of comparison.

It was possible to investigate the differences in the conduction mechanism between nanoceramics and conventional microcrystalline materials by studying the angular frequency dependence of the AC ionic conductivity, $\sigma(\omega)$, in EIS measurements. In most of electronic materials (semiconductors, solid electrolytes, etc.), it has been established that $\sigma(\omega)$ follows the "universal dielectric response" (or "universal dynamic response", UDR) law [147-149]:

$$\sigma(\omega) = \sigma_{DC} + A\omega^n \qquad (5)$$

where: σ_{DC} is the DC conductivity and A and n are temperature-dependent parameters. This law is a universal property of materials that is related to the dynamics of hopping conduction [147]. Its applicability to ionic conductors has been demonstrated by several authors for a large variety of materials, such as Na-β-Alumina [150], Nasicon-type materials [151, 152], ceramic oxides [149, 153], etc. Equation (5) can also be written as:

$$\sigma(\omega) = \sigma_{DC}*[1 + (\omega/\omega_p)^n] \qquad (6)$$

where: the reduced frequency, ω_p, is calculated by

$$\omega_p = (\sigma_{DC}/A)^{1/n} \qquad (7)$$

It has been proposed that the power, n, has a physical meaning [154] if n is greater than 1, the transport mechanism involves a localized hopping of the species with a small hop without leaving the neighborhood, while n smaller than 1 indicates a delocalized, translational motion with a big hop. This last case is typical for ionic conductors containing channels or layers in the crystal structure, allowing the fast migration of the carriers (Na-β-Alumina, NASICON-type materials, etc.) [150-153, 155]. Figure 15 shows the curves of $\sigma(\omega)$ vs. ω, obtained at 135 °C, and the corresponding fittings using equation (5) for all the samples. It can be clearly observed that the nanoceramics follow the UDR law. As it can be noted in Table II, n was found to be greater than 1 for microcrystalline CYO and CSO, indicating that the diffusion process of the mobile ions is based on the localized hopping in the vicinity of their initial site, as proposed in zirconia-based electrolytes [156]. Differently, for CYO and CSO

nanoceramics, n resulted much smaller than 1, showing that the ionic transport is dominated by delocalized carriers. Similar values were obtained for temperatures lower than the critical temperature at which the activation energy changes (hereafter called T_o). In addition, n also resulted smaller than 1 for the grain boundary (intergrain) conduction of the microcrystalline ceramics suggesting that the transport mechanism of the nanostructured samples involves the diffusion of the carriers through the grain boundaries. For temperatures higher than T_o, it was found that n increases with increasing temperature, until a value of 0.96 for CYO nanoceramics and of 0.83 for CSO nanoceramics, in both cases at temperatures about 230 °C (it is not possible to perform this analysis for higher temperatures because electrode reactions dominate the EIS spectrum). In the case of the bulk conduction of the microcrystalline materials, n decreases slowly with temperature, but keeping higher than 1 in the whole temperature range. The variation of n with temperature observed in the nanoceramics agrees with the change in the transport mechanism observed in the Arrhenius plots [147].

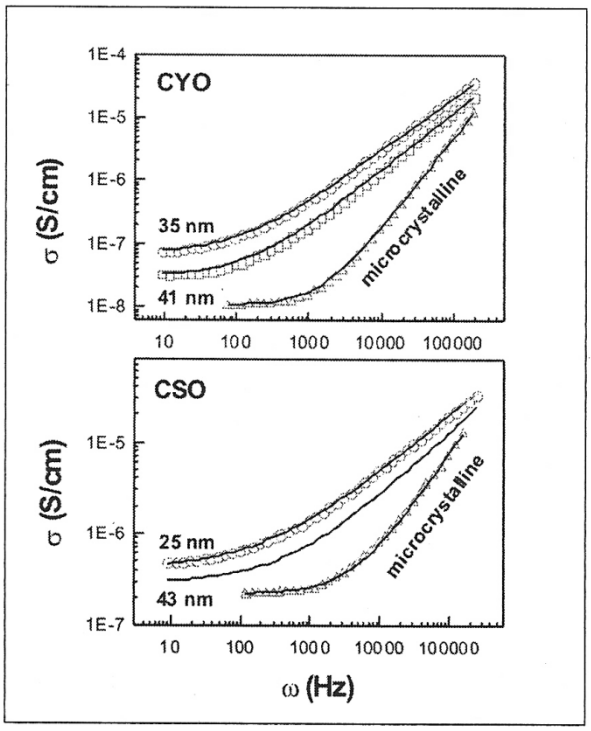

Fig. 15. Curves of ac conductivity σ vs angular frequency ω measured (symbols) at 135 °C and fitted (solid lines) with the UDR law (Eq. 5). Top: 35 nm (o),41nm(❑) and micrystalline (Δ) CYO. Bottom· 25 nm (o),43nm(❑) and micrystalline (Δ) CSO.

The DC conductivity of crystalline materials can be determined using the random walk theory [155]:

$$\sigma_{DC} = (Ne^2d^2\gamma/6kT)\,\omega_H \qquad (8)$$

where: N and e are the carrier concentration and charge, d is the characteristic hopping distance, ω_H is the hopping rate, γ is a geometrical factor, k is the Boltzmann's constant and T is the temperature. Almond and West proposed that ω_p can be identified as ω_p [156]. Even though this interesting suggestion is supported by several experimental studies, it has been a matter of intense debate and some generalizations have been proposed [157, 158]. However, several authors have used it as a tool for the investigation of the migration process in a large number of materials, among them [159-161]. In the following, with the above reservations, we will make the same assumption: $\omega_H = \omega_p$. In the case of nanostructured ionic conductors, the applicability of this formalism has not been clearly established yet, so this subject deserves further investigation. However, it is worth to mention that Nowick and Lim have suggested that it is valid when the ionic transport is dominated by free carries [157] which is the case of the nanoceramics studied in this work.

The values of ω_p [Hz] obtained by eq.(8) for the different CeO_2-based ceramics are summarized in Table II. Surprisingly, ω_p decreases with decreasing grain size in more than an order of magnitude compared to the values for bulk conduction in the microcrystalline materials. Then, assuming that $\omega_H = \omega_p$, the enhancement of the ionic conductivity in the nanoceramics is not related to an increase of the hopping rate.

The characteristic frequencies can be also investigated by studying the angular frequency dependence of the imaginary part of the electric modulus, M"(ω), or that of the imaginary part of the impedance Z"(ω). In case of conven-

Table II. Power of the UDR law n, reduced frequency (ω_p) as determined by Eq. (8) (which is assumed to be equal to the hopping rate) and the $Nd^2\gamma$ factor in Eq. (8) for the transport process of the CYO and CSO nanoceramics and for the bulk conduction in the microcrystalline materials

Samples	n	ω_p (Hz)	$Nd^2\gamma$ (cm^{-1})
CYO bulk	1.23	1060	$1.5\ 10^7$
CYO 41 nm	0.91	240	$1.4\ 10^8$
CYO 35 nm	0.85	130	$7.0\ 10^8$
CSO bulk	1.15	3900	$7.4\ 10^7$
CSO 43 nm	0.69	650	$5.7\ 10^8$
CSO 25 nm	0.63	250	$2.4\ 10^9$

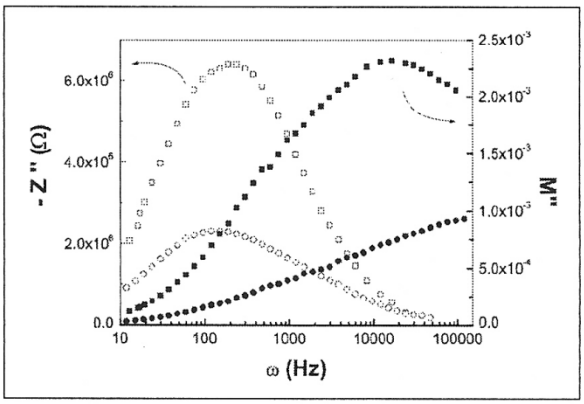

Fig. 16. -Z" and M" as a function of frequency, measured at 135°C, for the nanostructured CYO ceramics. Circles: 35 nm sample; squares: 41 nm sample.

tional microcrystalline ceramics, both curves exhibited similar characteristic frequencies as expected according to [162]. In contrast, the nanoceramics exhibited a different behavior, as it can be observed in Figure 16 for CYO nanoceramics. It is well-known that the frequency of the peak in M"(ω), n_M, represents a characteristic frequency of the conductivity relaxation. In Figure 16, it can be observed that n_M increases with decreasing grain size, as expected considering that the enhanced conductivity effect. However, it is worth to remark that n_M should not be identified as the hopping frequency [151]. The same holds for the frequency of the peak in Z"(ω), n_Z, in conventional microcrystalline materials. However, in the present case, it can be demonstrated that n_Z is close to the reduced frequency ω_P - determined from Eq. (7) - because the arc in the Nyquist plot is very flat. This is easy to be understood noting that, in the limit case in which Z" is negligible for the whole arc, $\sigma(\omega = n_Z)$ tends to $2\sigma_{DC}$, while $\sigma(\omega = \omega_p)$ is equal to $2\sigma_{DC}$ by definition. It can be observed that the values of n_Z determined from Figure 16 are in very good agreement with the values of ω_P presented in Table II.

Using the values of σ_{DC} and ω_P calculated from Eq. (5) and (7), it is possible to determine the factor $Nd^2\gamma$ in equation (8). It increases in a factor of 32 and 47 for CSO and CYO nanoceramics, respectively, compared to the values determined for bulk conductivity of the microcrystalline samples (see Table II). If it is assumed that the carrier concentrations in micro and nanoceramics are similar, it can be deduced that characteristic hopping distance increases in a factor of about 6-7 in the nanoceramics. Therefore,

Table III. Activation energies for conduction (E_a) and hopping (E_m) processes of nanoceramics and microcrystalline materials (in this last case, only the bulk conductivity data is presented)

Sample	E_a (eV)	E_m (eV)
CYO bulk	1,00	0,81
CYO 41 nm	0,86	0,83
CYO 35 nm	0,72	0,71
CSO bulk	0,87	0,78
CSO 43 nm	0,81	0,79
CSO 25 nm	0,74	0,72

the enhancement of ionic conductivity in the nanostructured CeO_2-based ceramics seems to be related to an increase of the hopping distance. However, a possible increase of N for decreasing grain size should also be considered, as it will be explained below.

According to Almond and West [156], the hopping rate is thermally activated:

$$\omega_H = \omega_{eff} \exp(-E_m/kT) \qquad (9)$$

where: E_m is the activation energy for the hopping process and ω_{eff} is an effective frequency. By replacing this expression for ω_H in Equation (9), it becomes apparent that E_a and E_m are equal only if the carrier concentration, N, is not thermally activated. For example, this is the case of free oxygen vacancies in oxide-anion solid electrolytes (observed in ceria and zirconia-based materials at high temperatures) [149, 160, 161]. Differently, if N is thermally activated, its activation energy should be added to E_m, increasing E_a. For ex., this occurs in the case of ceria and zirconia-based solid electrolytes at intermediate temperatures, since vacancies associate to doping cations and, therefore, the activation energy for the disassociation process must be considered [149, 160-161].

Table III summarizes the values of E_a and E_m for all the nano and microcrystalline samples studied in this work. Remarkably, both energies are almost equal for the nanoceramics for the low-temperature regime, while they differ in the case of the microcrystalline samples. This important result implies that free oxygen vacancies dominate the low-temperature conduction process in the nanostructured samples, while the dissociation energy cannot be neglected in the microcrystalline materials. The Arrhenius plot of ω_p for the CYO nanoceramic with smallest average grain size (35 nm) and for the CYO microcrystalline material shows that the slope is smaller

for the nanoceramic material, indicating that it has a lower E_m. The results of Table III also indicate that the association energy is lower for CSO materials, which explains the higher ionic bulk conductivity of these materials compared to that of CYO ceramics.

All the above results are consistent allowing to propose *a model for the transport process in the nanostructured ceria-based solid electrolytes: it is dominated by the delocalized hopping of free oxygen vacancies, which are probably located at grain boundaries*. Since the concentration of free vacancies is usually higher at the grain boundaries [161] and the grain boundary-to-bulk ratio increases for decreasing grain size, it is to be expected that the concentration of free oxygen vacancies increases for decreasing grain size, which could be partially responsible for the above mentioned increase of the $Nd^2\gamma$ factor.

Now, we shall discuss the nature of the transition observed in the conductivity measurements as a function of temperature. In most of thermally activated phenomena in physics, chemistry and biology, it has been found a simple relationship between the pre-exponential constant and E_a, known as the Meyer-Neldel rule or the compensation law. In the case of the ionic conductivity in solid electrolytes that satisfies the Arrhenius law [(eq. (4)], it can be expressed as [149,156]:

$$\ln (\sigma_o) = \alpha E_a + \beta \qquad (10)$$

where: α and β are constants. From the value of the slope, it can be defined a characteristic temperature, $T_d = (\alpha k)^{-1}$, which, in the case of metals, has been identified as the melting point [163]. For ionic conductors, it has been shown that T_d corresponds to an order-disorder transition in the mobile ion sublattice [156].

Figure 17 shows $\ln(\sigma_o)$ vs. E_a for the studied nanoceramics and also for the bulk and grain-boundary conductivities in the microcrystalline samples. For the samples with the lowest grain size, it has been included the data corresponding to both the high-temperature and low-temperature regimes. It can be noted an excellent linearity between both magnitudes. The values of T_d determined from the slope of the straight lines in Figure 17 resulted in excellent agreement with T_o, determined from the Arrhenius plot [91]. In the present case, T_d should be associated to a change in the transport mechanism, from the high-temperature, bulk-controlled conductivity to the low-temperature, grain boundary-controlled conductivity. In Figure 17, it can also be observed that the nanostructured samples correlate very well with the grain boundary transport, while, on the other hand, bulk diffusion mechanism does not fit with Mayer-Neldel curve. This accords with our statement that the ionic transport is controlled by grain boundaries in the nanostructured samples.

In summary, we have investigated *the ionic transport process in heavily-doped ceria-based nanoceramics proposing that it is based on the fast grain-boundary diffusion of free oxygen vacancies migrating with a delocalized translational motion with a big hop, differently to the case of conventional microcrystalline materials, for which the carriers exhibit a localized jump*. It was also studied the transition observed in the Arrhenius plots of the nanostructured ceria-based ceramics which is probably caused by a competition between the localized and delocalized carries in the transport mechanism. It is controlled by the bulk diffusion of localized oxide vacancies at intermediate temperatures, while free oxygen vacancies at the grain boundaries dominate the conductivity at low temperatures.

The present investigation on the transport mechanism in the studied nanoceramics opens the way for searching new ultrafast solid electrolytes, which could be very important from the technological point of view in order to reduce the operating temperatures of several devices, such as solid-oxide fuel cells, gas sensors, electrochemical reactors, solid-state batteries, etc.

4. Applications of nanostructured materials

From the numerous applications of the studied nanostructured materials at CINSO, we shall refer in the following to Gas Sensors and Solid Oxide Fuel Cells (operated at medium temperatures) IT-SOFCs, exhibiting both devices the most important advancement in their development.

4.1. *Gas Sensors built with Nanostructured Semiconductors*

We shall describe sensors built with semiconductive materials (for ex. SnO_2) detecting gases by the variation of surface resistance. The ceramic semiconductor previously reacts with the oxygen of air forming, at the semiconductor surface, oxygen adsorbates, such as O^-, O_2^-, O^{2-} [164]. These adsorbates which play an important role in the gas sensing (being the O^- the most active) are known to cover the semiconductor surface and grain boundaries and they react, at an operation temperature of ~300-450 °C if the sensor is built with a microcrystalline semiconductor. In case of *n*-type semiconductive metal oxides, the forma-

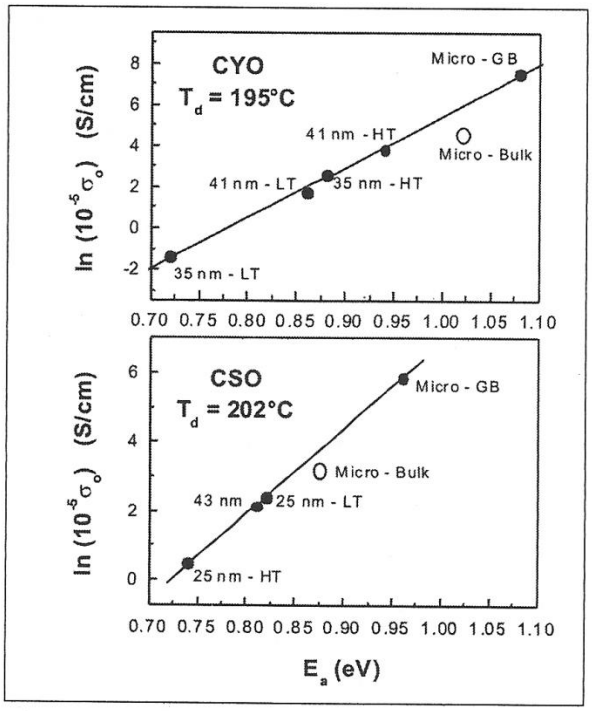

Fig. 17. ln (σ_0) vs Ea for the studied nanoceramics and the volume and grain boundary conductivity for the microcrystalline specimen. For samples with smaller grain size the data from the high and low temperature were included.

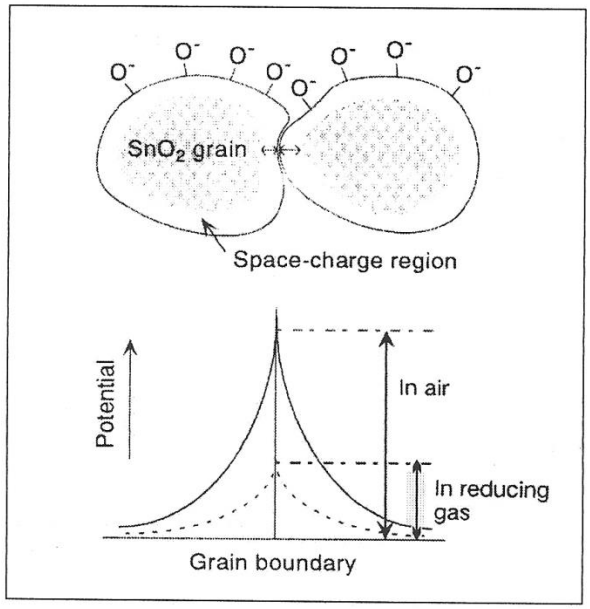

Fig. 18. A model of a potential barrier to electronic conduction at a grain boundary.

tion of these adsorbates builds a space-charge region, resulting in an electron-depleted surface layer (space-charge) due to the electron transfer to the adsorbates as follows:

$$1/2\ O_2(g) + 2e^- = 2O^- \text{ (adsorb.)} \qquad (11)$$

The depth of the space-charge (L) is a function of the surface coverage of oxygen adsorbates and of the intrinsic electron concentration in the bulk. The resistance of the *n*-type semiconductor is, in consequence high, because a potential barrier to electronic conduction is formed at each grain boundary [165] as shown in Figure 18. If the sensor is exposed to a reducing (or inflammable) gas (for ex. CO) at the operation temperature, the gas reacts with oxygen adsorbates according: to:

$$CO + O^- = CO_2 + e^- \qquad (12)$$

The oxygen adsorbates are consumed by the subsequent reactions, so that a lower steady-state surface coverage of the adsorbates is established, the potential barrier height decreases and a drop in resistance is produced. The resistance change is used as the measurement parameter of the semiconductor gas sensor. In general, the resistance variation ($\Delta\rho$) can be defined as $\Delta\rho$ = n.e.ΔL, where: n is the number of charges, e: charge of mobile species and L is the change of space-charge thickness. Otherwise, sensitivity (S) can be defined as:

$$S = R_{air} / R_{air + gas} \qquad (13)$$

where: R_{air} is the resistance in air and and $R_{air + gas}$ is the resistance in a sample gas containing a reducing component. The reactivity of the oxygen adsorbates is a function of the kind of reducing gas and the sensor temperature. In case of *n*-type semiconductor gas sensors in the presence of oxidizing gases (O_2 or NO_2 for ex.), the sensor resistance increases upon exposure to these gases as a result of their negatively charged chemisorption on the grain surfaces or boundaries. Consequently, sensitivity is a function of the amount of chemisorption, since oxygen adsorbates coverage on the surface remains constant.

Usually *n*-type semiconductive metal oxides are employed as sensor materials for a reducing gas detection. In case of *p*-type semiconductive metal oxides, the charge carriers are holes (positive) being then the resistance in air low because of the formation of negatively charged oxygen adsorbates. Otherwise, the extraction of electrons from the bulk enhances the holes concentration in the grain surface and boundaries. The consumption of oxygen adsorbates by reaction with the reducing gas leads to an increase of

the resistance which represents the reverse of *n*-type metal oxides behaviour.

Gas sensors were built at CINSO with microcrystalline and nanocrystalline semiconductive SnO_2, as it will be seen below. In every case, *it was observed that the sensitivity of sensors built with nanocrystalline material resulted always 30-37% higher than the one of sensors built with the microcrystalline conventional semiconductor and the operation temperature decreased to 180-220 °C for sensors with nanomaterial in comparison with usual temperature range: 350-450 °C for microcrystalline semiconductor.*

If a simple model is considered assuming that a sensor consists of a chain of uniform grains (with diameter D) connected by grain-boundaries, the core area presents a low resistance and the space-charge region (thickness: L) a high resistance as it is possible to observe in Figure 19, which shows the schematic models for grain-size effects [164]. In case of D >> 2L, there is a grain-boundary control. If D ≥ 2L, there is a neck control, since grains are connected by necks (usually ~ 0.8D) and if D < 2L, it appears that the active space-charge region is considerably major than the grain diameter and sensor becomes evidently more sensitive since a larger quantity of adsorbates can react with the gas to be detected. It is easy to conclude that sensor sensitivity increases as grain size decreases. Semiconductive metal oxides are used for sensors either pure or doped (doping contributes to increase the selectivity to certain gases) [165, 166].

Sensors to detect CO (g), VOCs (Volatile Organic Compounds) and hydrogen were built at CINSO with nanocrystalline tin oxide. As it was shown above, the sensor performance improves not only when D (grain diameter) decreases but also with increasing L (space-charge region thickness) since a major proportion of material interacts with the target gas, even if the grain size is not excessively small. These concepts were used to build a *sensor for CO (g) with nanocrystalline* SnO_2 [167]. The doping of SnO_2 with trivalent cations enabled to increase the response since the carriers concentration was reduced and, consequently, L increased. Doping of SnO_2 with Al_2O_3 enabled C. Xu et al. [166] to build sensors for H_2 detection but they did not report data on CO(g) sensing. They have prepared the semiconductive material by coprecipitation, followed by calcination at high temperature and could not evaluate the Al solubility in the SnO_2 lattice, in spite of reporting that it had to be lower than 1% as determined by resistivity measurements. The aim of Cabezas et al. work [167] was to study the possibility of increasing the Al solubility in the SnO_2 lattice because this fact could improve the gas sensor sensitivity since carriers concentration could decrease even more. Nanocrystalline SnO_2 was synthesised by the nitrate-citrate gel-combustion method [19, 20] since the use of similar routes in other systems made possible to increase the solubility limit of the dopant, in a metastable condition, while retaining the homogeneity in composition of materials [70, 110]. This is due to the fact that the powder is obtained by the rapid disintegration of the homogeneous gel, so the system cannot evolve towards its equilibrium state.

In Figure 20, the response of pure, 2 at% and 5 at% Al doped SnO_2 is plotted versus T(°C) for 200 ppm CO in air. If pure SnO_2 sensors were compared with 2 at% Al doped SnO_2 sensors, it was observed that the latter exhibited a higher sensitivity for the whole considered temperature range. The maximal sensitivity resulted: ~8 for non-doped SnO_2 and 10 for 2 at% Al doped SnO_2. The optimal working temperature (T_w) resulted ~ 375 °C for both types of sensors. However, 5 at% Al doped SnO_2 sensors exhibited a lower optimal working temperature: ~ 325 °C and their sensitivity resulted of 8. This decrease of T_w may be assigned to a shift of the characteristic formation temperature of adsorbates O^- by the incorporation of Al in the SnO_2 lattice. Results indicate that the gel-combustion method enables to increase the Al solubility in nanocrystalline SnO_2 in comparison with the co-precipitation method [167] and, at the same time, it reduces the crystallite size. Both facts improve the sensitivity of the sensors built with the gel-combustion synthesised nanomaterials as it was proved with the built thick film sensors. The response of the sensors reported in this work was considerably high, between 8 and 10 for 200ppm CO in synthetic air. Furthermore, it is possible to reduce

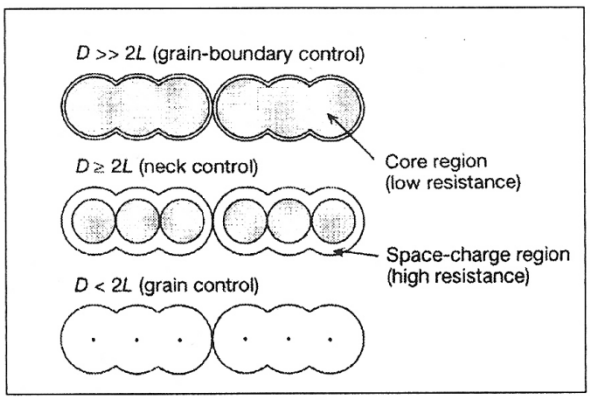

Fig. 19. Schematic models for grain size effects.

the operation temperature of sensors by increasing the Al concentration.

Thick film sensors with microcrystalline and nanocrystalline pure or In_2O_3-doped SnO_2 were built at CINSO [168] finding a major sensitivity (33-37%) in sensors built with doped nanocrystalline material with regards to those built with microcrystalline doped SnO_2. In case of nanocrystalline material, it was proved that crystallite size of pure or doped SnO_2 decreases if the doping concentration increases. Sensors performance improved for low In_2O_3 doping concentration (1% of the mass ratio Sn/In). It was demonstrated that a thermal treatment of 3 h at 700 °C was suitable to stabilise the sensor, which optimal working temperature resulted 270 °C (approximately 50 °C minor than that of sensors built with microcrystalline material). Sensitivity and response of sensors was determined for gas in thermal equilibrium with ethanol solutions (50, 500 ad 5000 ppm) in water, Figure 21 shows the resistance variation with time of a (1% In_2O_3 doped SnO_2) sensor in which it appears: the curve taken during the first functioning day of a non stabilised sensor (below) and that of the same sensor as measured on the second day after stabilisation treatment. Figure 22 is the response variation of a (1% In_2O_3 doped SnO_2) sensor for different ethanol concentrations (ppm) in air.

Another thick film sensing device, developed at CINSO as a result of performed research on nanocrystalline semiconductor SnO_2, was a *hydrogen sensor detecting 5 ppm H_2 in air* [169, 170]. Pure nanocrystalline SnO_2 was synthesized with a novel method developed at CINSO [169] by vigorous oxidation of $SnCl_2.2\ H_2O$ with H_2O_2 (30-250 vol.) obtaining an initial crystallite size of 1-2 nm and a final size of 5-6nm after sintering (as revealed, in both cases, by XRD peaks broadening with Scherrer technique). Figure 23 is the sensitivity versus the operation temperature (in °C) of the sensor for hydrogen. Sensitivity resulted 30-35% higher than that of sensors built with microcrystalline SnO_2 (as synthesised by the usual calcination method) and the highest sensitivity is reached at an operation temperature of ~ 180-200 °C. It is interesting to point out that commercial sensors as obtained with microcrystalline SnO_2 operate in a range 350-450 °C.

The three above described thick film sensors as well as the commercial sensors require a heater circuit to provide the adequate operation

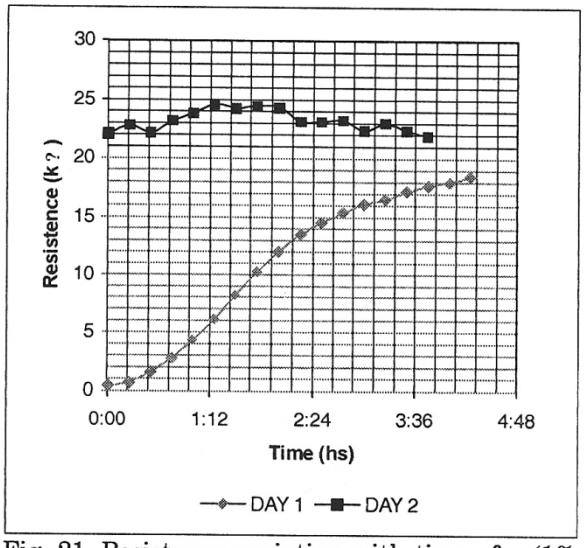

Fig. 21. Resistance variation with time of a (1% In_2O_3 doped SnO_2) sensor; curve of a non stabilised sensor (below) and of the same sensor after stabilisation treatment.

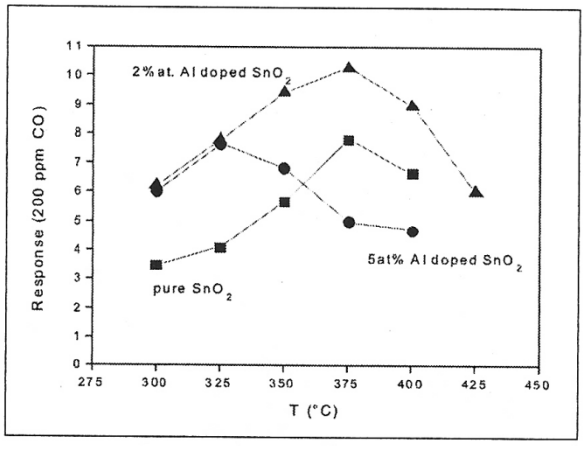

Fig. 20. Gas sensor response with pure, 2 at% and 5 at% Al-doped SnO_2 vs T(°C) for 200 ppm CO in air.

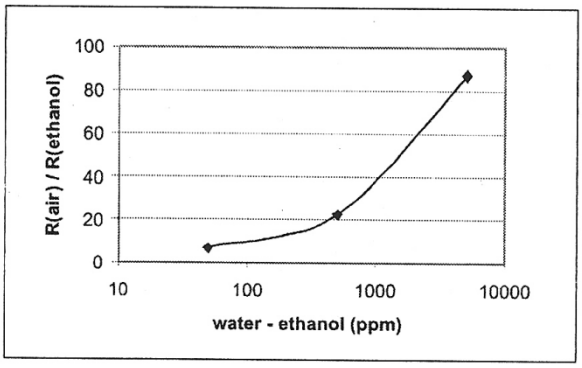

Fig. 22. Response variation of a (1% In_2O_3 doped SnO_2) sensor for different ethanol concentrations (ppm) in air.

temperature. Usually, conductive pastes are prepared with the metal oxide semiconductor and deposited by serigraphy on the top face of an electronic purity AlSiMg substrate (provided with two interdigitated Pt electrodes previously deposited by screen printing). In case of sensors built at CINSO, the conductive pastes were prepared with free of glass own formulations to reach the adequate tyxotropic properties required to deposit them by microelectronic techniques. On the bottom face is deposited a meandering Pt heater track also by microelectronic techniques.

An innovative heater and measurement device, developed at the Semiconductors Laboratory-CITEFA and CINSO, with MEMS technique (considered among the nanotechnology techniques [1]) was incorporated to one of the above described resistive sensors (sensor for hydrogen). This device consists of a Si micro-etched or micro-machined structure, Figure 24, similar to those used for thin film sensors [171, 172]. The micro-machined area is obtained by the wet-etching technique on a Si wafer coated with a N_xSi_x layer to stop the etching of the micromachining process and to provide a mechanical support. On the N_xSi_x layer, a Pt film is deposited in high vacuum and a double meander structure (heater-contacts system) is built with the lift-off technique. This circuit enables the commutation of the same Pt structure to be used as contact to extract the sensor signal or as heater. The ad-hoc necessary electronic circuit is detailed in Figure 25. The functioning principle of the associated electronics may be described as follows: the control logic is programmed with the PC (core of the system) to commutate the electrodes to act as heater or contacts. The sensor electrodes are excited through the Heater Block for a given time, providing the necessary power to activate the sensing nanocrystalline SnO_2 thick film. The film exhibits a thermal capacity enabling, once removed the feeding, to maintain the sensor temperature for a while (~ 1s). During this short time the circuit commutates the contact to Bias Block to excite the terminals with the adequate polarization levels. The PC acquires the data and the process is continually repeated.

With this new system [173], the same functional results of conventional heaters deposited on Si substrates are obtained but, using energy data from 10 to 15 times lower, which enables its application to portable equipments.

Before performing the above mentioned research on nanocrystalline SnO_2 and its application to the described resistive sensors, the study of *phenomena generated at the triple interface [nanocrystalline SnO_2/nanocrystalline ion-conducting oxide/gas]* was considered in the first PhD thesis on nanocrystalline materials performed in our country in the nineties [22]. Gas sensors (detecting ppm of CO) of two types resulted from this study [174] and they cannot be grouped with the above described sensors since they apply a new sensing way. Previous research considered the [Y-TZP/SnO_2] interface in contact with a reducing gas (CO). This interface used Y-TZP (yttria-stabilized tetragonal zirconia polycrystal with composition ZrO_2-2.8 mol% Y_2O_3) making possible to operate it at lower temperatures in comparison with the cubic FSZ (fully stabilized zirconia). The retention of this tetragonal phase was possible because it was a nanocrystalline material. Two identical nanostructured SnO_2 electrodes were deposited with a symmetrical geometry on both sides of the Y-TZP disk. In sensor of type I, the electrodes consisted of thick

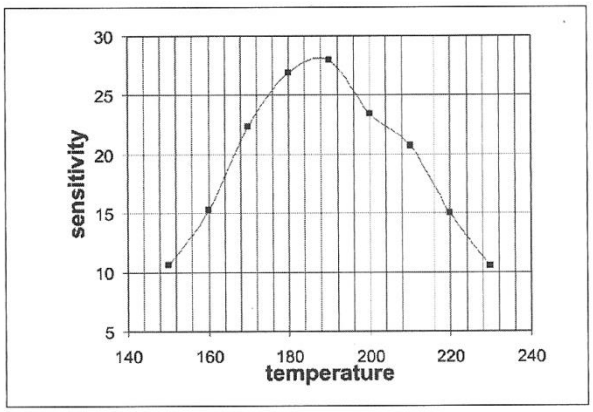

Fig. 23. Sensitivity (S) vs the operation temperature (°C) of the sensor for hydrogen.

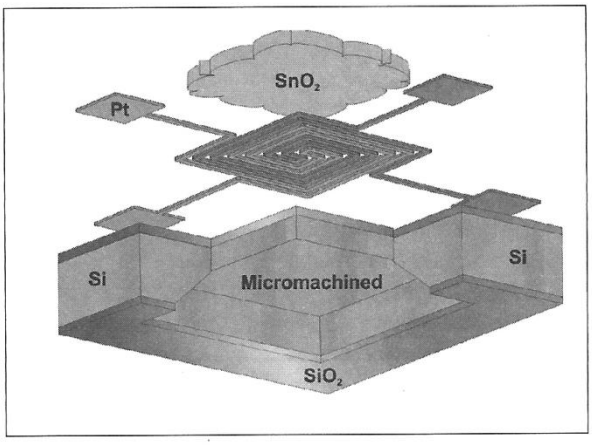

Fig. 24. (Si + N_xSi_y) micromachined structure.

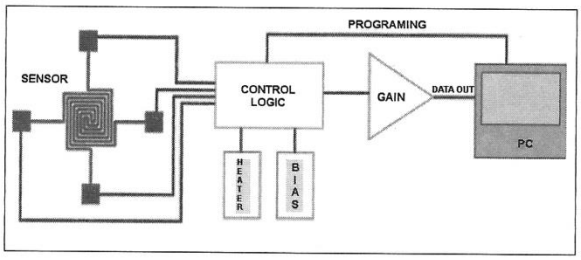

Fig. 25. Circuit enabling the commutation of the same Pt structure to be used as contact to extract the sensor signal or as heater.

films deposited by screen-printing from conductive SnO_2 paste and in the sensor of type II, the electrodes were SnO_2 deposited by flash-pyrolisis. The sensor I proved to detect from 50 to 350 ppm of CO in air in a temperature range from 400 to 550 °C with an optimal working temperature of 450 °C at a frequency of 6.3 Hz, as determined by EIS measurements. The sensors of type II detected between 10 and 350 ppm of CO in air in a temperature range 400-550 °C with an optimal operation temperature: 550 °C and a maximal frequency f = 0.10Hz or even smaller. In spite of exhibiting a higher operation temperature, sensors II resulted more sensitive than sensors I.

In spite of being the operation temperature of the nanosemiconductor lower than the usual working temperature (350-450 °C) in the conventional microcrystalline material, the ionic oxide required a higher temperature range to retain the tetragonal phase and this range of temperature was convenient to operate the interface as sensor.

4.2. *Fuel cells with nanostructured materials*

Fuel cells are electrochemical devices enabling to generate electrical energy from a chemical reaction, which generally is the water formation from H_2 and O_2. Solid oxide cells are detached because they replace H_2 by hydrocarbons, for ex. CH_4, as fuel. Conventional fuel cells use ceramic electrolytes, usually Y_2O_3 stabilized ZrO_2 (YSZ), in the cubic phase conducting at high temperature by the O^{2-} ion. The reduction reaction of O_2 to O^{2-} is produced at the cathode and, usually, manganites like (La; Sr)MnO_3 are used to catalyze it. In the anode, the fuel oxidation is produced and materials based on Ni are used to catalyze the reforming from CH_4 to H_2 and CO in presence of H_2O or CO_2:

$$CH_4 + H_2O \rightarrow 3H_2 + CO \qquad (14)$$

$$CH_4 + CO_2 \rightarrow 2H_2 + 2CO \qquad (15)$$

This process is known as *internal reforming* (it is produced in the same anode of cell). The resulting gases, H_2 and CO, react with the O^{2-} ions coming from the electrolyte to produce water and CO_2. *The main difficulty of these conventional SOFCs (Solid Oxide Fuel Cells) is that they must operate at temperatures from 900 to 1000 °C since the used materials to build them are efficient at high temperatures.* We shall refer in this review to high temperature fuel cells (HT-SOFCs) only as a reference to compare their performance with that of fuel cells developed at CINSO. It is obvious that nanomaterials are used for IT-SOFCs but they cannot be employed in conventional SOFCs, because of grain growth at high operation temperatures. *A considerable important research subject consists in looking for materials efficient at intermediate temperatures (500-700 °C).* Convenient materials were found for electrolytes, such as the Sm_2O_3, Gd_2O_3 or Y_2O_3 doped CeO_2 or (La;Sr)(Ga;Mg)O_3 perovskytes. In case of the cathode, numerous materials have been evaluated and, for example, it was found that several cobaltites [(La;Sr)CoO_3, (Sm;Sr)CoO_3] favour the O_2 reduction at intermediate temperatures. Otherwise, till now no completely adequate anodes have been found since the internal reforming requires of high temperatures. Consequently, new concepts are analyzed at the present, such as: SOFCs working by the direct oxidation of hydrocarbons [175, 177] or one-chamber cells like the cells presented in this work [178-184]. Usually, fuel and O_2 (air) are in separated chambers. However, Hibino et al. have proposed "one-chamber" solid oxide cells working in mixtures of hydrocarbons and air. These cells are based on the use of catalyzers which are selective for reactions in each electrode. In the anode, instead of the internal reforming, the environmental O_2 is used to produce the partial hydrocarbon oxidation. The reaction for CH_4 is:

$$CH_4 + \tfrac{1}{2}O_2 \rightarrow 2H_2 + CO \qquad (16)$$

Produced by the following reactions:

$$CH_4 + 2O_2 \rightarrow 2H_2O + CO_2 \qquad (a)$$

$$CH_4 + H_2O \rightarrow 3H_2 + CO \qquad (b)$$

$$CH_4 + CO_2 \rightarrow 2H_2 + 2CO \qquad (c)$$

Differently from the internal reforming, a probable solution is to catalyze the reaction (16) at intermediate temperatures.

In spite of the importance of one-chamber cells related to the possibility of simplifying the cell design (with the consequent weight de-

crease and cost reduction), there are still few publications confirming the reliability of these new devices [183, 184]. One-chamber cells, operated at high (HT) and intermediate (IT) temperatures, similar to those studied by Hibino et al. were evaluated at CINSO [185]. Synthesized and characterized (at CINSO) materials were used to build them. In spite of not reaching the high power density reported by Hibino et al., power density values resulted acceptable showing the possibility of generating energy in cells operated with hydrocarbons and air mixtures as fuel. In case of the one-chamber cells of this work functioning at high temperatures, new compound materials of NiO and ZrO_2-CeO_2 were used for anodes. The interest on these anodes is due to the fact that ZrO_2-CeO_2 materials are mixed conductors (conducting by O^{2-} ions and by e^-, due to the Ce^{4+} reduction to Ce^{3+}) in reducing atmosphere and by this fact, the oxidation reaction of fuel is produced on its whole surface while in electronic conductors occurs only in the [anode/electrolyte/gas] triple points. In consequence, in this work, the behavior of ZrO_2-CeO_2 solid solutions was studied in methane/air mixtures as catalyzers of the whole oxidation stage of fuel (reaction **a**).

Materials for both type of fuel cells (SOFCs and IT-SOFCs): ZrO_2-8 %mol Y_2O_3 and CeO_2-10 %mol Sm_2O_3 powders were synthesized by gel-combustion method using lysine as fuel. This is a novel route proposed at CINSO [23]. The resulting powders were characterized by X-ray diffraction (XRD). The crystallite mean size was determined with the Scherrer equation. The specific area was evaluated with the Brunauer-Emmett-Teller (BET) technique. Powders were used to prepare the electrolytes by uniaxial pressing and sintering at high temperature (1600-1700 °C for ZrO_2-Y_2O_3 ceramics and 1400-1500°C for CeO_2-Sm_2O_3 ceramics). These materials were characterized by XRD, density measurements, environmental scanning electron microscopy (ESEM) and electrochemical impedance spectroscopy (EIS).

Synthesis and structural characterization of ZrO_2-CeO_2 solid solutions ZrO_2-50, 70 and 90 %mol CeO_2 were synthesized by gel-combustion nitrate-glycine technique [110]. Phases were identified by XRD with synchrotron radiation experiments performed in the D12A-XRD-1 line of the Laboratorio Nacional de Luz Sincrotrón (LNLS, Campinas, Brasil) using an incident radiation with a wavelenght of 1.50060Å. A high intensity and low resolution configuration was used, without analyzer crystal in order to reach good statistics. Conventional XRD studies were also performed.

Study of redox and catalytic properties of ZrO_2-CeO_2 solid solutions was studied by Temperature Programmed Reduction (TPR) carried out with a conventional laboratory equipment provided with a thermal conductivity detector and a mixture of 4.5 % mol H_2/N_2 yield as reducing agent. Catalytic essays were performed in a conventional fix bed reactor, isothermally operated at atmospheric pressure. The feeding and the reactor efluent compositions were evaluated by on-line gaseous chromatography.

The building and evaluation of one-chamber solid oxide fuel cells was performed in high end intermediate temperature fuel cells:

- *High temperature one-chamber fuel cells:* YSZ (Yttria Stabilized Zirconia) was used for the electrolyte, $La_{0.8}Sr_{0.2}MnO_3$ (LSM) for the cathode. In case of the anode, NiO or ZrO_2-50, 70 or 90%mol CeO_2 compound material were used. Synthesis, structural and electrical characterization of all these materials are described elsewhere [185, 186]. For the cathode and the anode, conductive pastes were prepared with glycerine as solvent and painted on the surface of the electrolyte pellet (cylindrical shape: 8 mm diameter and 1 mm thick) after polishing both surfaces. LSM/YSZ/NiO cells were chosen as reference cells since their performance had been already informed in [178]. New anodes (developed at CINSO): NiO/ZrO_2-CeO_2 were prepared from NiO and ZrO_2-50, 70 or 90%mol CeO_2 mixtures in a 3:1 weight ratio.

- *Intermediate temperature one-chamber fuel cells:* CeO_2-10 %mol Sm_2O_3 (CSO) ceramics were prepared with powders obtained by the gel-combustion method. A based on NiO anode was used, forming a composite material with CSO (30% weight proportion) and PdO (7% weight concentration). PdO was chosen because it catalyzes the methane oxidation at intermediate temperatures [182]. These materials were synthesized by gel-combustion. Conductive pastes were got mixing the powders in the convenient proportion and using glycerine as solvent. $Sm_{0.5}Sr_{0.5}CoO_3$ (SSC) powders were synthesized by the liquid-mix method and calcined at 800°C to be used for cathodes. Glycerine was used as solvent for conductive pastes preparation. Sintering was made at 1000°C for 2 h.

- *Electrical evaluation of one-chamber fuel cells:* Cells were evaluated with an EG&G-PAR 273A galvanostat-potentiostat, for [air + CH_4] mixtures in proportions CH_4:O_2 of 1:1 to 2:1. The total gas flux was varied between 300 and 800 cm^3/min. Working temperature varied from 800 to 950 °C for high temperature cells and between 500 and 650 °C for intermediate tempera-

ture cells. Pt and Au wires were used as output terminals for anode and cathode, respectively.

With regards to the structural properties of the nanostructured homogeneous in composition ZrO_2-CeO_2 solid solutions used in IT-SOFCs, this subject was considered before in this article. Homogeneity in composition of the synthesized materials was observed and it is due to the used synthesis method since the system remains homogeneous during the process and the final combustion stage is too short, enabling the homogeneity retention in the resulting material.

Redox and catalytic properties of nanostructured homogeneous in composition ZrO_2-CeO_2 solid solutions are considered because they are tightly related to the IT-SOFCs performance. In this case, ZrO_2-50, 70 and 90 %mol CeO_2 powders, calcined at 600 °C and at 800 °C, were studied. The specific area values of the analyzed powders are reported in Table IV. It can observed that specific area data are similar with exception of that of ZrO_2-70 %mol CeO_2 specimen calcined at 600 °C. Containing Ce oxides can store oxygen if they are in contact with an oxidizing atmosphere and they can deliver oxygen if they are in a reducing atmosphere. This process is able by the redox Ce^{4+}/Ce^{3+} couple presence. Consequently, the solid reduction profile in a H_2 containing atmosphere is tightly related with this redox process and with the easy oxygen deliver. In Figure 26 the TPR profile of pure CeO_2 is shown. It is observed that reduction is produced in two steps. The maximal values appear at 380 and 800 °C, respectively. These data are similar to those reported by other authors [187]. The first peak involves the reduction of the surface sites and the second one the reduction of the solid bulk sites. TPR results of ZrO_2-CeO_2 specimen are reported in Table V.

It is possible to observe that for an equal composition, the calcination temperature slightly moves the TPR profile to the higher temperatures range. On the other side, a strong composition effect on the profiles is observed. Comparing the peaks position in Figure 26 with results of Table V, it is possible to conclude that the peak appearing at 380 °C (T1) for CeO_2 moves to lower temperatures for the ZrO_2-CeO_2 solid solutions showing that the reduction of surface sites was very favoured. A similar conclusion may be reached comparing the peak position at 800 °C for CeO_2 with the signals of higher temperature in the ZrO_2-CeO_2 (T3) specimen, then concluding that the ZrO_2 adding does not only improves the surface sites reduction but also the reduction of the bulk sites. In consequence, the Zr^{4+} presence in the solid structure has strongly changed the CeO_2 reducibility. Besides, the ZrO_2-90 %mol CeO_2 calcined at 600 °C and 800 °C specimen, show a third peak in the TPR profile, reported as T2 in Table V, appearing at 472 °C and 494 °C, respectively. These signals correspond to intermediate reducibility centers which can play an important role in the oxidation reactions.

The CH_4 conversion versus the reaction temperature is reported in Figures 27a and 27b. The results for calcined solids at 600 °C are shown in Figure 27a and results for the calcined at 800 °C specimen are reported in the Figure 27b. The CH_4 conversion at 500ºC for ZrO_2-90 %mol CeO_2 catalyzers calcined at 600 and 800 °C is 0.05 and 0.13, respectively and it is negligible for the ZrO_2-50 and 70 %mol CeO_2 specimen. The conversion values for the last specimen become important at higher temperatures. It is interesting to point out that, the formed products under the used working conditions of this work, were CO_2 y H_2O, being observed a good C equilibrium between the reactor input and output. In consequence, the formation of carbonous residues is discarded.

The ZrO_2-90 %mol CeO_2 catalyzers present mayor CH_4 conversion values than the other specimen in the whole temperature range used for these essays. The different behavior can-

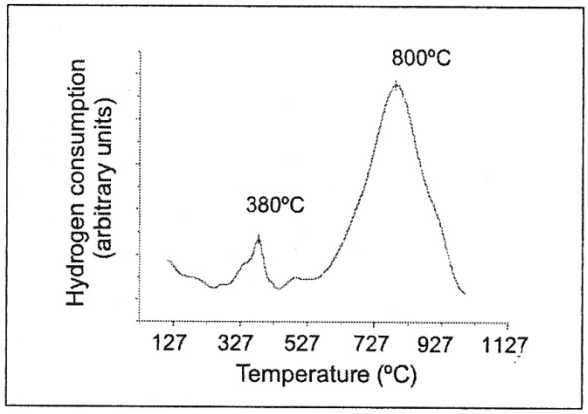

Fig. 26. Reduction profile at a programmed temperature for pure CeO_2.

Table IV. Specific area data of ZrO_2-50, 70 and 90mol% CeO_2 powders, calcined at 600°C and at 800 °C

Specimen	Specific area (m^2/g)
ZrO_2-50%CeO_2; 800 °C	31
ZrO_2-50%CeO_2; 600 °C	28
ZrO_2-70%CeO_2; 800 °C	30
ZrO_2-70%CeO_2; 600 °C	60
ZrO_2-90%CeO_2; 800 °C	28
ZrO_2-90%CeO_2; 600 °C	28

Table V. TPR profiles of ZrO_2- CeO_2 catalyzers

Specimen	T1	T2	T3
ZrO_2-50%CeO_2; 600 °C	187 °C	———	569 °C
ZrO_2-70%CeO_2; 600 °C	181 °C	———	530 °C
ZrO_2-90%CeO_2; 600 °C	108 °C	472°C	719 °C
ZrO_2-50%CeO_2; 800 °C	194 °C	———	582 °C
ZrO_2-70%CeO_2; 800 °C	247 °C	———	597 °C
ZrO_2-90%CeO_2; 800 °C	197 °C	494°C	747 °C

not be associated to differences in the specific areas because, as it was previously indicated, all the specimen present similar values of this parameter. On the other side, the TPR results for the ZrO_2-90 %mol CeO_2 solids have shown a third peak at intermediate temperatures, suggesting the existence of more labile oxygen ions in the structures, which could easily oxidize the CH_4.

Comparing the plotted results of Figures 27a and 27b, it is possible to conclude that the ZrO_2-90 %mol CeO_2 calcined at 800 °C specimen present a more convenient behavior than the calcined at 600 °C specimen and, consequently, it would be interesting to study the behavior of the first solid as anodic material in the one-chamber cells operated with CH_4. However, this fact was not possible since the electrodes built with this material were detached during the operation, probably due to a volume change induced by the Ce reduction. In consequence, ZrO_2-70 %mol CeO_2 catalyzers were used since, as it was mentioned before, the ZrO_2-70 %mol CeO_2 materials are degraded at high temperatures. It was necessary to use them with NiO compound materials because the electronic conductivity of the ZrO_2-CeO_2 solid solutions is not enough to collect the current. The study of the catalytic properties of the NiO/ZrO_2-CeO_2 compound materials for anodes is still running at the present.

In Figure 28a the discharge curves of one-chamber cells are shown. Cells were built with YSZ-Tosoh electrolyte (sintered at 1600 °C for 3 h), LSM as cathode and NiO and NiO/ZrO_2-70 %mol CeO_2 as anodes. Both curves were measured at 950 °C for mixtures with a CH_4 and O_2 rate of 1:1, which resulted the optimal mixture for both cells. In Figure 28b, power density versus current density curves are reported. Cells with NiO anode, already reported in the technical literature [178], enabled to adjust the cells building and the measurement conditions. In spite of not reaching the maximal expected power density (121 mW/cm^2), the measured value of this work (39 mW/cm^2) is acceptable considering that the electrodes were prepared with analytical purity regents.

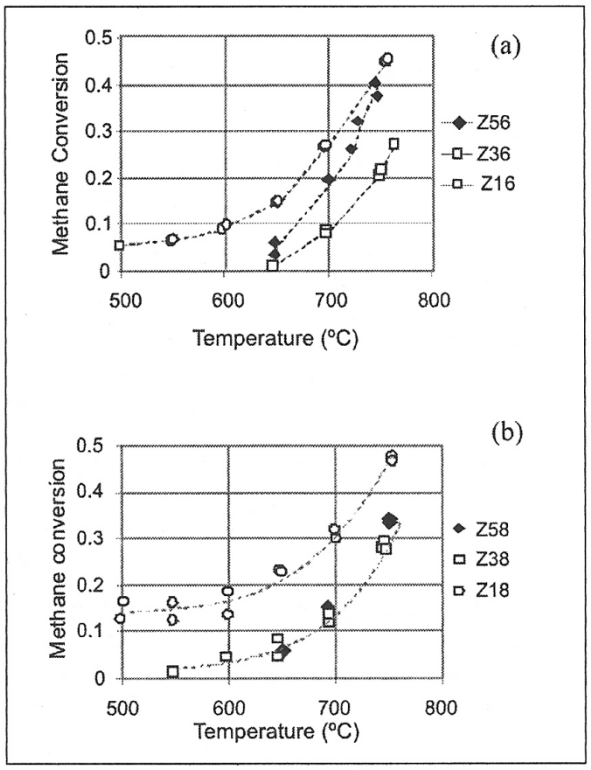

Figs. 27a. and 27b. Methane conversion vs. Reaction temperature for ZrO_2-50, 70 and 90 %mol CeO_2 calcined at 600 °C (a) and 800 °C (b) powders.

Severe adhesion difficulties were found for NiO/ZrO_2-CeO_2 anode, not only during the cells building but during their operation too. This fact is already known and reported in the literature and it is due to the expansion produced when the Ce transform from Ce^{4+} to Ce^{+3} in reducing atmosphere [185, 186]. These difficulties were more important in case of ZrO_2-90 %mol CeO_2 solid solutions. On the other side, as it was already discussed, the ZrO_2-50 %mol CeO_2 solid solutions loose their homogeneity in composition at 950°C or even at higher temperatures. By this reason, it was decided to study cells with NiO/ZrO_2-70 %mol CeO_2 anode (sintered at 1000°C for 1.5 h to avoid the degradation of the used solid solution).

It resulted also difficult to take out current with the proposed anode being this fact probably due to the low electronic conductivity of ZrO_2-CeO_2 materials. Though in Ref. [183], it is not reported this difficulty for NiO/CeO_2-Sm_2O_3 anode (with weight proportions similar to those of this work), as it was mentioned before, it was

decided to deposit a porous Pt film on the anode as current collector in place of a Pt mesh (this process is known and reported in the literature [188]) enabling to solve the above mentioned problem. Figures 28a and 28b corresponding to the cell with NiO/ZrO_2-70 %mol CeO_2 anode were measured in this way. As it can be observed, this anode exhibits a better performance in comparison with the NiO anode, enabling to reach a maximal power: 53 mW/cm², meaning an improvement of 36%.

This performance improvement of the cells with NiO/ZrO_2-CeO_2 anode, in comparison with those with NiO anode, is due to the excellent catalytic properties of the ZrO_2-CeO_2 solid solutions for the total CH_4 oxidation in O_2 presence. The H_2O and CO_2 favour the CH_4 reforming of the non reacted methane (due to the NiO presence), generating H_2 and CO in a more efficient way. In consequence, the power density of the cell increases. The catalytic properties of the NiO/ZrO_2-CeO_2 compound material for anode are still studied at present.

With regards to the preparation and electrical properties of CeO_2-Sm_2O_3 solid electrolytes for intermediate temperature IT-SOFCs. The CSO powders, as synthesized by gel-combustion, only exhibited the expected fluorite type cubic phase with a crystallite mean value of 10 nm. A high specific area of 30 m²/g was measured for calcined at 400 °C powders. It is important to point out that the proposed gel-combustion synthesis route with nitrate-lysine as fuel was applied to synthesize CSO powders for the first time in this work. Ceramics prepared from above described powders by uniaxial pressing and sintering at temperatures between 1400 and 1500 °C, exhibited high relative densities, between 98 and 100%. Studies of EIS showed a considerable grain-boundary resistance, in spite of their excellent relative density. CSO electrolyte was used to build one chamber IT-SOFCs. The electrodes were synthesized from analytical purity reagents. Once again, the current collectors were based on porous Pt and Au films for anode and cathode, respectively. Figure 29a shows the discharge curve of a one-chamber cell operated at intermediate temperature, with SSC cathode, CSO electrolyte and NiO-CSO-PdO anode, measured at 600 °C for fuel mixtures with a CH_4:O_2 ratio of 2:1. Figure 29b presents the power density versus current density curves for the same cell. The maximal power density was 97mW/cm².

It is important to discuss the usefulness of adding PdO to the anode. As it is reported in [179, 180], the use of conventional anodes based on NiO (i.e. NiO/CSO) is not sufficient to reach

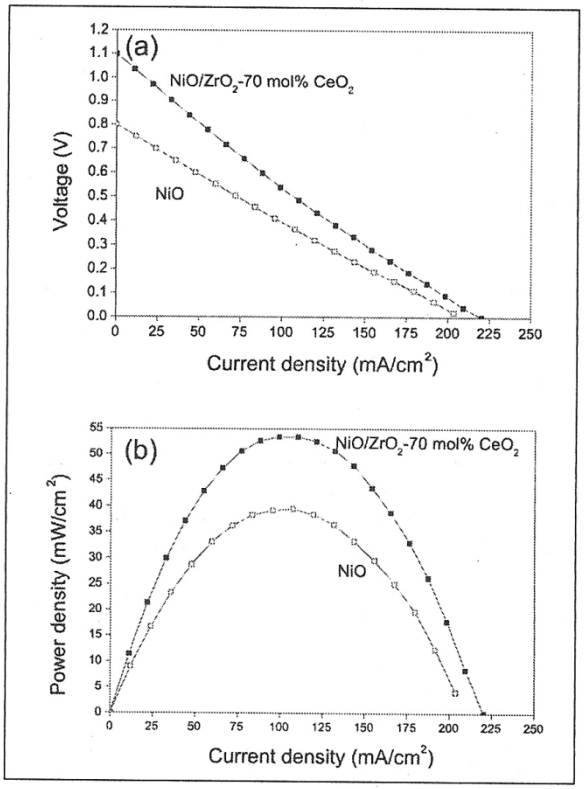

Figs. 28 a. and 28b. Voltage versus Current density (a) and Power density versus Current density (b) for HT-fuel cells with NiO and NiO/ZrO_2-70%mol CeO_2 anodes, operated at 950°C in CH_4 + air mixture (CH_4:O_2 ratio of 1:1).

high voltage and power density values if the cell is operated with CH_4 and at temperatures lower than 700 °C. The PdO addition enables to catalyze the CH_4 partial oxidation at intermediate temperatures, forming H_2 and CO which react with the O^{2-} anions coming from the electrolyte. Besides, it is important to point out that, differing from the case of HT-SOFCs, there are not papers, with exception of [185], confirming the possibility to reach high power densities for intermediate temperature cells as Tomita et al. [182] have reported, indicating this fact the importance of the present results.

Actually, an experimental one-chamber IT-SOFC (Figure 30) was built at CINSO and its evaluation is in process. It consists of a nanostructured ceria-based electrolyte, ZrO_2-CeO_2 mesoporous anode impregnated with an adequate catalyzer and using cobaltites or ferro-cobaltites nanotubes as cathode [189]. Larrondo et al [93] synthesized mixed Zr and Ce oxides of nominal composition $Ce_{0.9}Zr_{0.1}O_2$ by the gel-combustion method using glycine as fuel [187] so as to obtain materials with nanometric particles. Ceria and

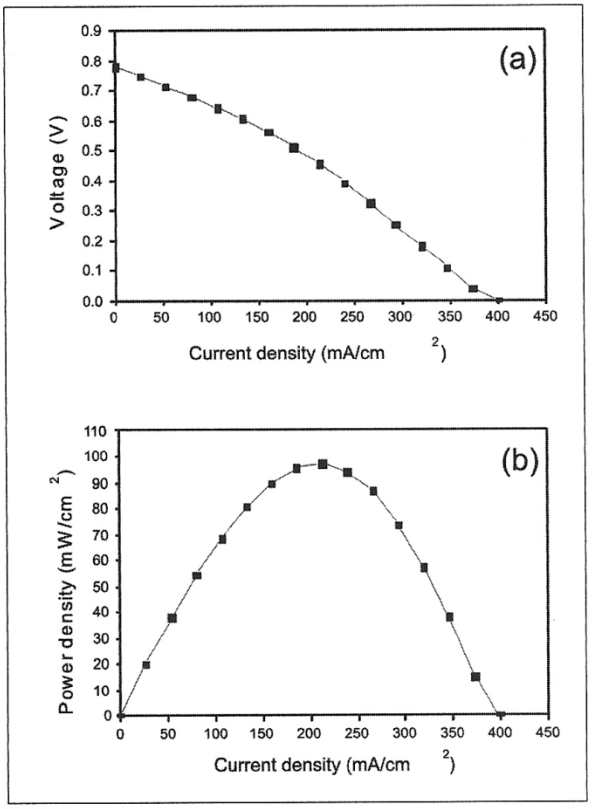

Figs. 29a. and 29b. Voltage versus Current density (a) and Power density versus Current density (b) for one chamber [SSC/CSO/NiO-CSO-PdO] IT-fuel cell, operated at 600°C in a CH_4 + air mixture [CH_4:O_2 ratio of 1:1).

ZrO_2-CeO_2 oxides were chosen by their structural en electronic properties which make them useful as catalyzers [188-190]. Besides, ceria is able to storage oxygen because of cerium cation capability to easily change between their reduced and oxidized states (Ce^{3+}/Ce^{4+}). The synthesized material was impregnated with a Ni solution so as to reach 9% and 50% (w/w). Catalyzers were characterized (evaluating texture, structure and catalytic behavior) in the reaction of methane partial oxidation. It was that synthesis method was effective because materials exhibited good morphologic characteristics (specific area, composition and homogeneity). Otherwise, catalyzers resulted active, showing a stable behavior during the operation period and showing a methane conversion of 90% for temperatures between 500 and 700 °C, being hydrogen and CO the main observed products.

5. Conclusions

The aim of this review is to report the sequential steps of the Nanostructured Materials Project which is performed at CINSO-CONICET-CITEFA, being this purpose presented in the Introduction of this article. In this part, nanomaterials are introduced and defined and references to their unusual properties are given.

In the Experimental Methodology Part, a review on the synthesis of nanoceramics is exposed, including the preparation of solid ionics (solid electrolytes) and electrode materials (even perovskite nanotubes and mesoporous materials)

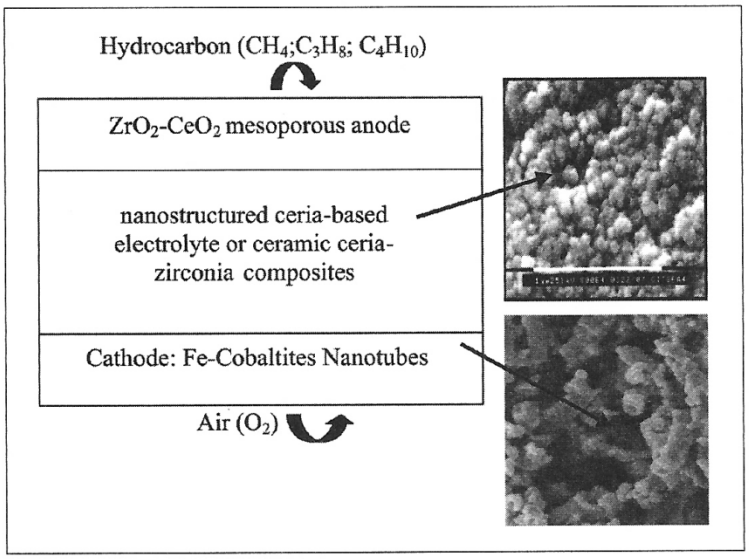

Fig. 30. Experimental one-chamber IT-SOFC built at CINSO.

for solid oxide fuel cells and semiconductors (II-VI metallic oxides) for gas sensors and optoelectronic devices. Several synthesis methods of nanostructured materials are described, classifying them by the process used for their preparation. Several papers on synthesis methods are reported.

Characterization techniques are briefly described reporting the main used approaches, such as: conventional X-ray diffraction, Rietveld refining method of crystallographic parameters, Scherrer peak broadening technique to evaluate the nanomaterials particle size, BET (Brunauer-Emmett-Teller) method to determine the surface area and the electron microscopies (SEM, TEM and even HRTEM) to study the nanostructure of these materials.

SAXS (Small Angle X-Ray Scattering) EXAFS (Extended X-Ray Absorption Fine Structure) are other mentioned interesting tools for characterization using the synchrotron radiation; numerous articles on the subject are reported. Other physical characterization techniques for nanomaterials as electron diffraction or positron annihilation spectroscopy are only mentioned. Methods of chemical characterization are briefly described. A list of general papers on the mentioned or described techniques is given.

The results of synthesised nanostructured materials at CINSO are described in the third part of the article and they are mainly referred to the gel-combustion preparation method which is particularly described. In the first PhD thesis on nanocrystalline materials performed in our country in the nineties, the study of phenomena produced at the triple interface [nanocrystalline semiconductor (SnO_2)/nanocrystalline ion-conducting oxide (Y-TZP)/ gas] was performed (being Y-TZP: Yttria-stabilized Tetragonal Zirconia Polycrystal and the gas: CO). The retention of the metastable tetragonal Y-TZP phase was possible because it was a nanocrystalline material according to mechanism afterwards described. Both materials: SnO_2 and Y-TZP were synthesised at CINSO by the gel-combustion method. Several papers are reported on these subjects. Gel-combustion technique was also used to prepare novel calcia-stabilized TZP nanoceramics, ZrO_2-Al_2O_3 and CeO_2-Y_2O_3, to synthesize compositionally homogeneous nanocrystalline ZrO_2-35 mol% CeO_2 powders or ZrO_2-15 mol% CeO_2 nanopowders, to prepare solid electrolytes for fuel cells (ZrO_2-Y_2O_3 and ZrO_2- Sc_2O_3). The different use conditions (starting reagents, fuels, temperature, etc.) of this method were studied in a second PhD work completely devoted to gel-combustion. Otherwise, the nanosemiconductor SnO_2 was synthesized at CINSO for the first time. Another semiconductor, ZnO, was synthesized by gel-combustion and dip-coating methods in order to evaluate the optical properties variation with the crystallite size.

Special synthesis methods for functional nanomaterials with a determined morphology were developed at CINSO, such as cobaltite ($La_{0.6}Sr_{0.4}CoO_3$-LSCO) nanotubes, to be successfully used for high performance cathodes for IT-SOFCs (Solid Oxide Fuel Cells operated at Intermediate Temperature) due to its significant mixed ionic-electronic conductivity in this temperature range. The performance of LSCO nanotubes was advantageous in comparison with that of tubular structures formed by assembling manganite nanoparticles nanotubes. Another special nanomaterials synthesis method was used for Ni catalyzers to produce the catalytic oxidation of methane in anodes of one-chamber IT-SOFCs. CeO_2 and CeO_2-ZrO_2 were chosen by their convenient structural and electronic properties.

In the paragraph of the 3.2 Part of this article, characterization results of nanostructured materials synthesized at CINSO are described. Usual characterization techniques included: conventional XRD, measurement of the mean crystallite size by the broadening of XRD diffraction peaks (Scherrer technique), Rietveld refining method, BET specific area and observation techniques to study the crystallites morphology (ESEM-Environmental Scanning Electron Microscopy, TEM, HRTEM and SEM). In case of electrical characterization of ionic materials EIS (Electrochemical Impedance Spectroscopy) was required. Besides, nanosemiconductors characterization also included: grazing incidence XRD, reflectivity (XRR) and grazing incidence low angle diffusion (GISAXS) techniques. In the particular case of the metastable t"-form of the tetragonal phase ZrO_2-10mol% Y_2O_3 powders was found using the Hyperfine characterization - Perturbed Angular Correlations technique and in case of compositionally homogeneous nanocrystalline ZrO_2-CeO_2 solid solutions, the usual characterization was completed with Raman spectra analysis.

The supporting nanomaterial for Ni-catalyzers ($Ce_{0.9}Zr_{0.1}O_2$) was characterized by BET (specific area and total volume of pores) and the carbon content analysis by a flash combustion followed by chromatography. Templates were tested by Temperature Programmed Reduction-TPR. The consumed H_2 (reducing agent) was evaluated by thermal conductivity detector (TCD).

A wide bibliography of results on synthesis and characterization of the nanomaterials (published at CINSO) is given.

for solid oxide fuel cells and semiconductors (II-VI metallic oxides) for gas sensors and optoelectronic devices. Several synthesis methods of nanostructured materials are described, classifying them by the process used for their preparation. Several papers on synthesis methods are reported.

Characterization techniques are briefly described reporting the main used approaches, such as: conventional X-ray diffraction, Rietveld refining method of crystallographic parameters, Scherrer peak broadening technique to evaluate the nanomaterials particle size, BET (Brunauer-Emmett-Teller) method to determine the surface area and the electron microscopies (SEM, TEM and even HRTEM) to study the nanostructure of these materials.

SAXS (Small Angle X-Ray Scattering) EXAFS (Extended X-Ray Absorption Fine Structure) are other mentioned interesting tools for characterization using the synchrotron radiation; numerous articles on the subject are reported. Other physical characterization techniques for nanomaterials as electron diffraction or positron annihilation spectroscopy are only mentioned. Methods of chemical characterization are briefly described. A list of general papers on the mentioned or described techniques is given.

The results of synthesised nanostructured materials at CINSO are described in the third part of the article and they are mainly referred to the gel-combustion preparation method which is particularly described. In the first PhD thesis on nanocrystalline materials performed in our country in the nineties, the study of phenomena produced at the triple interface [nanocrystalline semiconductor (SnO_2)/nanocrystalline ion-conducting oxide (Y-TZP)/ gas] was performed (being Y-TZP: Yttria-stabilized Tetragonal Zirconia Polycrystal and the gas: CO). The retention of the metastable tetragonal Y-TZP phase was possible because it was a nanocrystalline material according to mechanism afterwards described. Both materials: SnO_2 and Y-TZP were synthesised at CINSO by the gel-combustion method. Several papers are reported on these subjects. Gel-combustion technique was also used to prepare novel calcia-stabilized TZP nanoceramics, ZrO_2-Al_2O_3 and CeO_2-Y_2O_3, to synthesize compositionally homogeneous nanocrystalline ZrO_2-35 mol% CeO_2 powders or ZrO_2-15 mol% CeO_2 nanopowders, to prepare solid electrolytes for fuel cells (ZrO_2-Y_2O_3 and ZrO_2- Sc_2O_3). The different use conditions (starting reagents, fuels, temperature, etc.) of this method were studied in a second PhD work completely devoted to gel-combustion. Otherwise, the nanosemiconductor SnO_2 was synthesized at CINSO for the first time. Another semiconductor, ZnO, was synthesized by gel-combustion and dip-coating methods in order to evaluate the optical properties variation with the crystallite size.

Special synthesis methods for functional nanomaterials with a determined morphology were developed at CINSO, such as cobaltite ($La_{0.6}Sr_{0.4}CoO_3$-LSCO) nanotubes, to be successfully used for high performance cathodes for IT-SOFCs (Solid Oxide Fuel Cells operated at Intermediate Temperature) due to its significant mixed ionic-electronic conductivity in this temperature range. The performance of LSCO nanotubes was advantageous in comparison with that of tubular structures formed by assembling manganite nanoparticles nanotubes. Another special nanomaterials synthesis method was used for Ni catalyzers to produce the catalytic oxidation of methane in anodes of one-chamber IT-SOFCs. CeO_2 and CeO_2-ZrO_2 were chosen by their convenient structural and electronic properties.

In the paragraph of the 3.2 Part of this article, characterization results of nanostructured materials synthesized at CINSO are described. Usual characterization techniques included: conventional XRD, measurement of the mean crystallite size by the broadening of XRD diffraction peaks (Scherrer technique), Rietveld refining method, BET specific area and observation techniques to study the crystallites morphology (ESEM-Environmental Scanning Electron Microscopy, TEM, HRTEM and SEM). In case of electrical characterization of ionic materials EIS (Electrochemical Impedance Spectroscopy) was required. Besides, nanosemiconductors characterization also included: grazing incidence XRD, reflectivity (XRR) and grazing incidence low angle diffusion (GISAXS) techniques. In the particular case of the metastable t"-form of the tetragonal phase ZrO_2-10mol% Y_2O_3 powders was found using the Hyperfine characterization - Perturbed Angular Correlations technique and in case of compositionally homogeneous nanocrystalline ZrO_2-CeO_2 solid solutions, the usual characterization was completed with Raman spectra analysis.

The supporting nanomaterial for Ni-catalyzers ($Ce_{0.9}Zr_{0.1}O_2$) was characterized by BET (specific area and total volume of pores) and the carbon content analysis by a flash combustion followed by chromatography. Templates were tested by Temperature Programmed Reduction-TPR. The consumed H_2 (reducing agent) was evaluated by thermal conductivity detector (TCD).

A wide bibliography of results on synthesis and characterization of the nanomaterials (published at CINSO) is given.

In the 3.3. Paragraph the first of the two research works: Metastable Phases Retention in Nanostructured Materials is considered. The different phases of the pure ZrO_2 are carefully described. The high temperature tetragonal and cubic phases retention at lower temperatures (even at T_{room}) by doping with metal oxides (MO or M_2O_3) to form solid solutions with zirconia, is considered. Doping oxides (Y_2O_3, CaO, MgO) with lower valence state cations than Zr^{4+} create vacancies in the oxygen sublattice, favoring their conduction. The compositional range for the stabilisation of the tetragonal and/or cubic phases is narrow and depends on temperature and doping. Besides, these structures can be retained in case of ceramics exhibiting a mean grain size lower than a critical value. For ex., it was found that in case of ZrO_2-Y_2O_3 ceramics, the critical size varies from 0.2 to 1mm for 3 mol% Y_2O_3 compositions. In the special case of CeO_2 doping (with a doping cation valence state equal to that of Zr^{+4}) the mechanisms of t and c phases stabilization result controversial. It is pointed out the advantage of retaining the tetragonal phase stabilization at intermediate temperature to use these materials as electrolytes for IT-SOFCs. Otherwise, it is not convenient to retain the low temperature stable phase (monoclinic) because it is a bad conducting form.

Doped zirconia: ZrO_2-Y_2O_3, ZrO_2-MgO, ZrO_2-CaO and ZrO_2-CeO_2 systems are reviewed and the equilibrium phase diagrams of different systems are included to clarify the appearing phases. Conditions under which the retention of metastable phases is produced in each system, synthesis methods to prepare the different phases, chemical composition, critical crystallite size and crystallographic properties of retained phases are introduced and discussed. New retained phases were reported at CINSO using different characterisation techniques and a wide bibliography on these subjects is given. Data are compared with those of the scarce technical literature.

In the 3.4. Paragraph: Fast Ionic- Transport in Nanostructured Oxide-Ion Solid Electrolytes is considered. The electrical properties of nanostructured heavily yttria or samaria-doped ceria ceramics were studied as a function of grain size by electrochemical impedance spectroscopy. A remarkable enhancement in the total ionic conductivity, of about one order of magnitude, was found in nanostructured samples compared to the intrinsic bulk conductivity of these materials as evaluated in conventional microcrystalline ceramics. This effect is attributed to the predominance of grain boundary conduction in the nanostructured materials, coupled with an increase in the grain boundary ionic diffusivity with decreasing grain size. It was shown that, at low temperatures, the total ionic conductivity of nanostructured heavily doped ceria solid electrolytes increases in about one order of magnitude compared to that of conventional microcrystalline materials. This result is attributed to the predominance of the grain boundary conductivity in the nanostructured ceramics. It was also found that the enhancement of the total ionic conductivity is associated to a reduction of the activation energy, probably caused by an increase in the grain boundary ionic diffusivity with decreasing grain size. For the samples with the smallest average grain sizes (35-50 nm), a change in the transport mechanism as a function of temperature was established, which is attributed to a transition from bulk-controlled (at high temperatures) to grain boundary-controlled (low temperatures) ionic conduction.

Afterwards, an enhancement of the total ionic conductivity in nanostructured heavily-doped ceria dense pellets has been found. It was showed at CINSO that the total ionic conductivity increases in about one order of magnitude in these nanoceramics compared to the intrinsic bulk conductivity of these materials, evaluated in conventional microcrystalline ceramics. We also showed that the impedance spectra observed for nanoceramics is very different to that generally found for conventional microcrystalline materials. The different behavior, also observed in other phenomena dominated by grain boundaries, strongly suggests the predominance of grain boundary conduction in nanoceramics. In agreement with literature results it was found that the activation energy E_a is lower for the nanoceramics than for microcrystalline materials. It is proposed that the enhancement of the total ionic conductivity can be accounted for due to the raise of the parallel grain boundary conductivity in the nanostructured samples, coupled to an increase of the grain boundary ionic diffusivity with decreasing grain size. It is proposed a mechanism that it is based on the fast grain-boundary diffusion of free oxygen vacancies that migrate with a delocalized translational motion with a big hop, differently to the case of conventional microcrystalline materials, for which the carriers exhibit a localized jump. A transition is observed in the Arrhenius plots at ~ 190 °C of the nanostructured ceria-based ceramics and it is probably caused by a competition between the localized and delocalized carries in the transport mechanism. It is controlled by the bulk diffusion of localized oxide vacancies at intermediate temperatures, while

free oxygen vacancies at the grain boundaries dominate the conductivity at low temperatures. This investigation on the transport mechanism in nanoceramics opens the way for searching new ultrafast solid electrolytes, which could be very important from the technological point of view in order to reduce the operating temperatures of several devices, such as solid-oxide fuel cells, gas sensors, electrochemical reactors, solid-state batteries, etc.

4. Part deals with the Applications of the studied nanoceramics: in 4.1 Part, for Gas Sensors. The mechanism by which gas sensors built with semiconductive materials (for ex. SnO_2) detect gases by the variation of surface resistance is described. Nano-semiconductive metal oxide, either pure or doped (doping contributes to increase the selectivity to certain gases) is used to build thick film type gas sensors: to detect CO (g) [Al doped SnO_2], VOCs (Volatile Organic Compounds) [In doped SnO_2] and hydrogen [pure SnO_2]. In every case, the sensor sensitivity results 30-37% higher in comparison with that of sensors built with the microcrystalline conventional semiconductor and the operation temperature decreases to 180-220 °C in the first case in comparison with the usual operation temperature range: 350-450 °C for sensors built with a microcrystalline semiconductor. As the development of these gas sensors is original, applications for patents are presented and some of them are still in study. The sensor to detect hydrogen, built with pure, non-doped SnO_2 and provided with a contact conmutation circuit which can measure alternatively the resistance variation (sensor measurement) and the operation temperature, generated two patents applications: the first referred to a new synthesis method to prepare the pure nanocrystalline SnO_2 (which still in process) and the second: the patent of the sensor itself (which was already granted). The text also refers to a new way of sensing developed at CINSO (which patent is in process). It is a sensor to detect ppm of CO(g) by the variation of some parameters at the triple interface [nano-ionic oxide/nano-semiconductive oxide/gas] when the gas is adsorbed.

In 4.2. Paragraph: Fuel Cells with nanostructured materials are described. SOFCs electrolyte and electrode materials were synthesized and their structural, electrical and catalytic properties have been evaluated giving details of these processes and numerous references on reasearch performed at CINSO. Analysis and characterization of these materials reveal their excellent charactheristics to be used in high and intermediate temperature cells. Conventional two chamber SOFC cells, built with conventional microcrystalline materials, operating at high temperature (800-1100 °C) are carefully described to compare its performance with that of SOFC type cells, built with nanocrystalline materials and operating at intermediate temperature (550-750 °C). Otherwise, the advantages of using one-chamber fuel cells, either functioning at high or low temperature ranges are discussed. Results of literature for one chamber HT-SOFCs are discussed and compared with results of one-chamber IT-SOFCs. The latter fuel cells have been built with materials completely synthesised and characterised at CINSO to work in methane and air mixtures. Their evaluation and shown results confirmed the possibility to reach considerably high power densities even for intermediate temperature cells. In this case, the addition of PdO to the anode resulted important to favour the methane oxidation. Actually, an experimental one-chamber IT-SOFC was built at CINSO and its evaluation is in process. It consists of a nanos-tructured ceria-based electrolyte, ZrO_2-CeO_2 mesoporous anode impregnated with an adequate catalyzer and using cobaltites or ferro-cobaltites nanotubes as cathode.

6. Acknowledgements

This work was sponsored by the YPF Foundation (2003 Repsol-YPF Award and several bourses CONICET-YPF and "José Estenssoro" for young researchers) and by the ANPCyT-Agencia Nacional de Promoción Científica y Tecnológica (Grant: PICT N° 10-14268). XRD research performed with synchrotron radiation were sponsored by the LNLS - Laboratorio Nacional de Luz Sincrotrón (Brasil, Project D12A-XRD1-1857) inside the frame of the CAPES-SECyT cooperation between Brasil and Argentina (Project BR/PA02-EVI/016). Sincere thanks are given to all the members of CINSO (researchers, technicians, students and secretary) since without their effort and work this project could not be possible; so my sincere thanks are given to Dr. Diego G. Lamas (who revised this review and directed a considerable part of this project, Dr. Horacio R. Cánepa, Dr. Rodolfo O. Fuentes, Dr. Aldo F. Craievich, Dra. Marcia C. de Abreu-Fantini, Dr. Rogério Junqueira Prado, Dra. Alicia B.Trigubó, Dr.Ricardo Aragón, Dr. Jorge R. Casanova, Lic. Eduardo A. Heredia, Ing. Ma. E.F.de Rapp, Lic. Rosa E. Baby, Analist. Sistem. Mario F. Bianchetti, Analist. Sistem. Marcelo D. Cabezas, Dr. Martín Bellino, Tco. Raúl D'Elía, Dra.Valeria Messina, Ing. Ma. Cristina Distéfano, Dra. Susana A. Larrondo, Dr. Gustavo E. Lascalea, Dr. Ulises Gilabert, Dra.Liliana Fraigi,

Tco. Alejandro Fernández, Dra. Laura Sánchez, Dr. Joaquín Sacanell, Lic. Ismael Fábregas, Lic. y Magister Claudia Bojorge, Ing. Ana María Martínez, Ing. Paula M. Abdala, Lic. Leandro M. Acuña, Ing. Genoveva Zimicz, Lic. Eugenio Otal, Lic. Fernando F. Muñoz, Tco. Hugo Bravo. Special thanks are given to Mrs. Mirta Rinaldi de Pullano for her continuous assistance to the whole CINSO staff and collaborators.

7. References

[1] M. C. Roco, JOM-J. *Minerals, Metals and Materials*, 54 (2002) 22.
[2] H. Gleiter, *Prog. Mater. Sci.*, 33 (1989) 223.
[3] H. Gleiter, *Adv, Mat.*, 4 (1992) 474.
[4] A. Henglein, *Chem. Rev.*, 89 (1989) 1061.
[5] H. Weller, *Angew. Chem.* Int. Ed. Engl. 32 (1993) 41.
[6] H. Gleiter, *Acta Mater.* 48 (2000) 1.
[7] J. V. Stark, D. G. Park, I. Lagadie, K. J. Klabunde, *Chem. Mat.*, 8 (1996) 1904.
[8] J. V. Stark, K. J. Klabunde, *Chem. Mat.*, 8 (1996) 1913.
[9] Y. Sun, Y. Xia, *Science*, 298 (2002) 2176.
[10] O. B. Koper, K. J. Klabunde., *Chem. Mat.* 9 (1997) 2481.
[11] C. Monty, *Nanostruct. Mater.* 1 (1993) 450-475.
[12] *"Interfacial Effects and Novel Properties of Nanomaterials"*, Ed. W. Lojkowski y J. Blizzard, Scitec Publications Ltd., Zürich, Suiza (2003).
[13] *"Nanomaterials, Synthesis, Properties and Applications"*, Ed. A. S. Edelstein, R. C. Cammarata, Institute of physics Publishing, Bristol y Philadelphia, USA (1997).
[14] D. H. Pearson, A.S. Edelstein, *Nanostruct. Mater.*, 11 (1999) 1111.
[15] G. González, J. A. Freites, C. E. Rojas, *Scr. Mater.*, 44 (2001) 1883.
[16] P. Taneja, R. Chandra, R. Banerjee, P. Ayyub, *Scr. Mater.*, 44 (2001) 1915.
[17] D. G. Lamas, G. E. Lascalea, N. E. Walsöe de Reca, *J. Eur. Ceram. Soc.* 18 (1998) 1217.
[18] R. E. Juárez, D. G. Lamas, G. E. Lascalea, N. E. Walsöe de Reca, *J. Eur. Ceram. Soc.* 20 (2000) 133.
[19] L. B. Fraigi, D. G. Lamas, N. E. Walsöe de Reca, *Nanostruct. Mater.* 11 (1999) 311.
[20] L. B. Fraigi, D. G. Lamas, N. E. Walsöe de Reca, *Mater. Lett.* 47 (2001) 262.
[21] L. B. Fraigi, D. G. Lamas, N. E. Walsöe de Reca, in "Microsensores de Estado Sólido para Monitoreo de Medio Ambiente". Programa CYTED (Ciencia y Tecnología para el Desarrollo), Proyecto IX.2, Ed. Control S.R.L., Bs. As. (1999), pag. 57-72.
[22] D. G. Lamas, *PhD Thesis* (Physics), FCEyN-Universidad de Buenos Aires (1999).
[23] G. E. Lascalea, *PhD Thesis* (Science and Technology of Materials), Instituto de Tecnología "Prof. Jorge A. Sábato", UNSAM (2004).
[24] "Nanostructures and Nanomaterials- Synthesis, Properties & Applications", Ed. G. Cao, Imperial College Press, London (2004).
[25] J. C. Brinker, J. W. Scherer, "Sol-Gel Processing: The Physics and Chemistry of Sol-Gel Processing", Academic Press, Boston (1990).
[26] A. C. Pierre, "Introduction to Sol-Gel Processing", Kluwer Academic Press, Boston (1998).
[27] J. Ying, *J. Aerosol Sci.*, 24 (1993) 315.
[28] S. W. Chung, J. Yu, J. R. Heath. Appl. Phys. Lett., 76 (2000) 2068.
[29] H. P. Klug, L. E. Alexander, "X-Ray Diffraction Procedures for polycrystalline and amorphous Materials", Wiley Interscience Publication, New York (1974).
[30] D. Balzar, "Defect and Microstructure Analysis from Diffraction", , Oxford University Press, London, New York (1999).
[31] A. Guinier, G. Fournet, "Small Angle Scattering of X-Rays", John Wiley &Sons, New York (1955).
[32] J. Rouquerol, F. Rouquerol, K. S. W. Sing, "Absorption by Powders and porous Solids", Academic Press, London (1999).
[33] T. Allen, "Particle Size Measurement", Vol. I, Kluwer Academic Press, Netherlands (1999).
[34] L. B. Fraigi. *Doctoral Thesis* (Engineering), FI-Universidad de Buenos Aires (2006).
[35] Th. E. Weirich, M. Winterer, S. Seifried, H. Hahn, F. Fuess, *Ultramiscroscopy*, 81 (2000) 263.
[36] R. Würschum, G. Soyez, H. E. Schaefer. *Nanostruct. Mater.*, 3 (1993) 225.
[37] T. Haubold, R. Birringer, B. Lengeler, H. Gleiter, *Phys. Lett.* A, 135 (1989) 461.
[38] S. de Panfilis, F. D´Acapito, V. Haas, H. Konrad, J. Weissmüller, F. Boscherini, *Phys. Lett.* A, 207 (1995) 397.
[39] *"EXAFS Spectroscopy, Technique and Applications"*, Ed. B. K. Teo, D. C. Joy, Plenum Press, New York (1980).
[40] R. E. Juárez, D. G. Lamas, R. Gastien, G. E. Lascalea, N. E. Walsöe de Reca, *Proceed. "9° Congr. Intern. de Cerám." - "3° Congr. MERCOSUR de Cerám."* Olavarría (Bs. As.) 27-29th May.1998), 349.
[41] R. E. Juárez, D. G. Lamas, G. E. Lascalea, N. E. Walsöe de Reca, *An. Asoc. Quím. Arg.* 84 (1996) 303.
[42] D. G. Lamas, R. E. Juárez, M. F. Bianchetti, G. E. Lascalea, L. B. Fraigi, N. E. Walsöe de Reca, *Proceed. SAM-CONAMET-AAS 2001,* Posadas (Misiones), 12-14th. Sept., 2001, Vol. III, 905.
[43] G. E. Lascalea, D. G. Lamas, N. E. Walsöe de Reca, L. Pérez, E. Cabanillas, *Proceed. SAM-CONAMET- Symp. Materia 2003,* San Carlos de Bariloche (Río Negro) 17-21st. Nov., 2003, 816.
[44] A. Fernández, D. G. Lamas, R. Kempf, R. O. Fuentes, E. D. Cabanillas, N. E. Walsöe de Reca, A. F. Craievich, *Proceed. SAM-CONAMET 2005,* Mar del Plata (Bs. As.) 18-21st. October, 2005, paper 299 (ed. CD).
[45] L. B. Fraigi, D. G. Lamas, N. E. Walsöe de Reca, *Proceed. "9° Congr. Intern. de Cerám." - "3° Congr. del Mercosur de Cerám.",* Olavarría (Bs. As.) 27-29th. May, 1998) 341.
[46] L. B. Fraigi, D. G. Lamas, N. E. Walsöe de Reca, *Química Analítica* (España) 18 (1999) 71.
[47] L. B. Fraigi, R. E. Juárez, D. G. Lamas, G. E. Lascalea, N. E. Walsöe de Reca, in *"Aplicaciones*

Interdisciplinarias de Materiales", Ed. J. P. Adrados, J. L. Aragón, M. Torres, Publish. by de la Torre, Madrid, Spain (2002), pag. 7-20.

[48] L. B. Fraigi, D. G. Lamas, N. E. Walsöe de Reca, *Materials Letters,* 47 (2001) 262-266.

[49] D. G. Lamas, R. E. Juárez, A. Caneiro, N. E. Walsöe de Reca, *Nanostruct. Mat.* **10** (1998) 1199.

[50] D. G. Lamas, G. E. Lascalea, G. Alejandro, R. E. Juárez, N. E. Walsöe de Reca, *Proceed. SAM' 97,* Tandil (Bs. As.) 14-16th, May, 1997, 455.

[51] M. F. Bianchetti, R. E. Juárez, D. G. Lamas, N. E. Walsöe de Reca, L. Pérez, E. Cabanillas, *J. Mat. Res.* 17 (2002) 2185.

[52] D. G. Lamas, R. E. Juárez, G. E. Lascalea, N. E. Walsöe de Reca, *J. Mat. Sci. Lett.,* 20 (2001) 1447.

[53] G. E. Lascalea, D. G. Lamas, L. Pérez, E. D. Cabanillas, N. E. Walsöe de Reca, *Mat. Lett.* 58 (2004) 2456.

[54] G. E. Lascalea, D. G. Lamas, E. Djurado, E. D. Cabanillas, N. E. Walsöe de Reca, *Mat. Res. Bull.* 40 (2005) 2029.

[55] R. E. Juárez, D. G. Lamas, G. E. Lascalea, N. E. Walsöe de Reca, *Anales AFA* **6**, 307.

[56] R. Kempf, D. G. Lamas, A. Fernández, L. Pérez, S. González, G. E. Lascalea, N. E. Walsöe de Reca, *Proceed. SAM-CONAMET 2005,* Mar del Plata (Bs. As.) 18-21st.October, 2005), paper 303 (ed. CD).

[57] P. M. Abdala, R. Kempf, D. G. Lamas, *ECS Trans - Solid Oxide Fuel Cells,* 7 (2007) 2197.

[58] Z. L. and Z. C. Kang, "Functional and Smart Materials-Structural Evolution and Structure Analysis", Plenum Press, New York (1998).

[59] C. D. Bojorge, H. R. Cánepa, U. E. Gilabert, D. Silva, E. A. Dalchiele, R. E. Marotti, *J. Mat.Sci.-Mater. Electron.*18 (2007) 1119.

[60] C. D. Bojorge, E. H. Otal, H. R. Cánepa, N. E. Walsöe de Reca, *Proceed. SAM-CONAMET 2007,* San Nicolás (Bs. As.) 4-7th Sept. 2007.

[61] M. G. Bellino, J. G. Sacanell, D. G. Lamas, A. G. Leyva, N. E. Walsöe de Reca, *J. Am. Chem. Soc.* 129, 11 (2007) 3066.

[62] M. G. Bellino, *PhD Thesis* (Physics), FCEyN-Universidad de Buenos Aires (2007).

[63] P. Levy, A. G. Leyva, H. E. Troiani, R. D. Sánchez, *Appl. Phys. Lett.* 83 (2005) 5247.

[64] A. G. Leyva, P. Stoliar, M. Rosebusch, V. Lorenzo, P. Levy, C. Albonetti, M. Cavallini, F. Biscarini, H. E. Troiani J. Curiali, R. D. Sánchez, *J. Sol. Stat. Chem.* 177 (2004) 3949.

[65] L. Hueso, N. Mathur, *Nature,* 427 (2004) 301.

[66] S. J. Skinner. *Int. J. Inorg. Mater.* 3 (2001) 113.

[67] S. A. Larrondo, M. A. Vidal, B. Irigoyen, A. F. Craievich, D. G. Lamas, I. O. Fábregas, G. E. Lascalea, N. E. Walsöe de Reca, N. Amadeo, *Catalysis Today* 107-108 (2005) 53.

[68] A. Boudghene-Stambouli, E. Traversa, *Sust. Energy Rev.*, 6 (2002) 433.

[69] R. E. Juárez, D. G. Lamas, G. E. Lascalea, N. E. Walsöe de Reca, *Def. and Dif. Forum* 177-178 (1999) 1.

[70] D. G. Lamas, N. E. Walsöe de Reca, *J. of Mat. Sci.* 35 (2000) 5563-5567.

[71] D. G. Lamas, G. E. Lascalea, R. E. Juárez, N. E. Walsöe de Reca, *Proceed. SAM 2000,* Neuquén, 16-18th. August, 2000) 925.

[72] I. O. Fábregas, J. R. Casanova, M. P. Basílico, G. E. Lascalea, D. G. Lamas, R. Kempf, N. E. Walsöe de Reca, A. F. Craievich, C. V. Santilli, *Proceed. CONAMET-SAM 2006,* Santiago de Chile, 28th. Nov.- 1st. Decemb., (2006), paper p3 (ed. CD).

[73] I. O. Fábregas, D. G. Lamas, R. O. Fuentes, M. E. Fernández de Rapp, N. E. Walsöe de Reca, A. F. Craievich, *Activity Rep. Braz. Synchr. Light Lab.,* (2004) paper 396. (ed. in CD).

[74] D. G. Lamas, R. O. Fuentes, I. O. Fábregas, G. E. Lascalea, M. E. Rapp, J. R. Casanova, N. E. Walsöe de Reca, A. F. Craievich, M. C. A. Fantini, *Proceed. CONAMET-SAM 2004,* La Serena, Chile, 3-5th. November, 2004) 775.

[75] D. G. Lamas, *2005 Activity Rep. Braz. Synchr. Light Lab.*, Science Highlights (2005) 24.

[76] D. G. Lamas, R. O. Fuentes, I. O. Fábregas, M. E. Fernández de Rapp, G. E. Lascalea, J. R. Casanova, N. E. Walsöe de Reca, A. F. Craievich, *J. Appl. Cryst.* 38 (2005) 867.

[77] M. C. Caracoche, J. A. Martínez, P. C. Rivas, A. M. Rodríguez, D. G. Lamas, G. E. Lascalea, N. E. Walsöe de Reca, *J. of the Am. Cer. Soc.,* 88 (2005) 1564-1567.

[78] P. Scardi, M. Leoni, D.G. Lamas and E.D. Cabanillas, *Powder Diffract.* 20 (2005) 353.

[79] I. O. Fábregas, R. O. Fuentes, D. G. Lamas, M. E. Fernández de Rapp, N. E. Walsöe de Reca, M. C. A. Fantini, A. F. Craievich, R. P. Millen, M. L. A. Temperini, *J. of Phys.: Condens. Matt.* 18 (2006) 7863.

[80] D. G. Lamas, R. O. Fuentes, M. E. Fernández de Rapp, J. R. Casanova, I. O. Fábregas, G. E. Lascalea, N. E. Walsöe de Reca, A. F. Craievich, M. C. A. Fantini, *Activity Rep. Brazil. Synchr. Light Lab.,* (2003) paper 147 (ed. in CD).

[81] R. O. Fuentes, D. G. Lamas, I. O. Fábregas, J. R. Casanova, M. E. Fernández de Rapp, N. E. Walsöe de Reca, M. C. A. Fantini, A. F. Craievich, *Activity Rep. Brazil. Synchr. Light Lab.* (2003) paper 157 (ed. in CD).

[82] I. O. Fábregas, R. O. Fuentes, D. G. Lamas, M. E. Fernández de Rapp, N. E. Walsöe de Reca, M. C. A. Fantini, A. F. Craievich, *Activity Rep. Brazil. Synchr. Light Lab.,* (2004) paper 496 (ed. in CD).

[83] I. O. Fábregas, D. G. Lamas, L. M. Acuña, R. O. Fuentes, M. E. Fernández de Rapp, N. E. Walsöe de Reca, M. C. A. Fantini, A. F. Craievich, R. J. Prado, *Activity Rep. Brazil. Synchr. Light Lab.,* (2005) paper 705 (ed. in CD).

[84] L. M. Acuña, D. G. Lamas, R. O. Fuentes, I. O. Fábregas, P. M. Abdala, M. E. Fernández de Rapp, N. E. Walsöe de Reca, M. C. A. Fantini, A. F. Craievich, R. J. Prado, *Activity Rep. Brazil. Synchr. Light Lab.* (2005) paper 738 (ed. in CD).

[85] J. R. Casanova, I. O. Fábregas, D. G. Lamas, G. E. Lascalea, N. E. Walsöe de Reca, A. F. Craievich, C. V. Santilli, *Activity Rep. Brazil. Synchr. Light Lab.,* (2005) paper 743 (ed. in CD).

[86] I. O. Fábregas, D. G. Lamas, R. O. Fuentes, M. E. Fernández de Rapp, N. E. Walsöe de Reca, A.

F. Craievich, M. C. A. Fantini, *Proceed. SAM-CONAMET 2005,* Mar del Plata, 18-21st. October, 2005, paper 298 (ed. in CD).
[87] J. R. Casanova, I. O. Fábregas, D. G. Lamas, N. E. Walsöe de Reca, G. E. Lascalea, R. Kempf, A. F. Craievich, C. V. Santilli, *J. of Appl. Crys.,* 40 (2007) 147.
[88] J. Novotny (editor), "Science of Ceramics Interfaces II", Elsevier Science, Amsterdam (1994).
[89] W. E. Lee and W. M. Rainforth, *"Ceramic Microstructures, Property Control by Processing"*, Chapman and Hall, London (1994).
[90] R. C. Garvie, R. H. J. Hannink and R. T. Pascoe, *Nature*, 258 (1975) 703.
[91] M. G. Bellino, D. G. Lamas, N. E. Walsöe de Reca, *Adv. Func. Mater.* 16 (2006) 107.
[92] M. G. Bellino, D. G. Lamas, N. E. Walsöe de Reca, *Adv. Mater.* 18 (2006) 3005.
[93] D. Lamas, M. Cabezas, I. O. Fábregas, N. E. Walsöe de Reca, G. Lascalea, A. Kodjaian, M.Vidal, N. Amadeo, S. Larrondo *ECS Transactions,* 7 (2007) 961.
[94] J. D. McCullough, K. N. Trueblood, *Acta Cryst.* 12 (1959) 507.
[95] D. K. Smith, H. W. Newkirk, *Acta Cryst.* 18 (1963) 983.
[96] G. Teufer, *Acta Cryst.* 15 (1962) 1187.
[97] D. K. Smith, C. F. Cline, *J. Am. Ceram. Soc.* 45 (1962) 249.
[98] A. H. Heuer, V. Lanteri, S. C. Farmer, R. Chaim, R.R. Lee, B. W. Kibble, R. M. Dickerson, *J. Mat. Sci.* 24 (1989) 124.
[99] S. P. S. Badwal, *Solid State Ionics,* 52 (1992) 23.
[100] F. F. Lange, *J. Mat. Sci.* 17 (1982) 240.
[101] J. S. Lee, J. I. Park, T. W. Choi, *J. Mat. Sci.* 31 (1996) 2833.
[102] M. Yashima, K. Ohtake, M. Kakihana, M. Yoshimura, *J. Mat. Sci. Lett.* 13 (1994) 1564.
[103] M. Yashima, M. Kakihana, H. Ishii, Y. Ikuma, M. Yoshimura, *J. Mat. Sci.* 11 (1996) 1410.
[104] S. Rossignol, F. Gérard, D. Duprez, *J. Mat. Chem.* 9 (1999) 1615.
[105] P. C. Rivas, M. C. Caracoche, J. A. Martínez, A. M. Rodríguez, R. Caruso, N. Pellegri, O. De Sanctis, *J. Mat. Res.* 12 (1997) 493.
[106] R. Caruso, E. Benavídez, O. De Sanctis, M. C. Caracoche, P. C. Rivas, M. Cervera, A. Caneiro, A. Serquis, *J. Mat. Res.* 12 (1997) 2594.
[107] R. Muchillo, N. H. Saito, N. S. Muccillo, *Mat. Lett.* 25 (1995) 165.
[108] M. Yashima, K. Ohtake, M. Kakihana, M. Yoshimura, *J. Am. Ceram. Soc.* 77 (1996) 2773.
[109] O. Yokota, M. Yashima, M. Kakihana, A. Simofuku, M. Yoshimura, *J. Am. Ceram. Soc.* 82 (1999) 1333.
[110] D. G. Lamas, G. E. Lascalea, R. E. Juárez, E. Djurado, L. Pérez, N. E. Walsöe de Reca, *J. of Mat. Chem.* 13 (2003) 904.
[111] G. E. Lascalea, D. G. Lamas, E. Djurado, N. E. Walsöe de Reca, *The J. of the Arg. Chem. Soc.,* 91 (2003) 135.
[112] E. Zhou, S. Bhaduri, S. B. Bhaduri, *NanoStruct. Mat.* 18 (1997) 653.
[113] S. Bhaduri, S. B. Bhaduri, *NanoStruct. Mat.* 18 (1997) 755.
[114] A. K. Shulka, V. Sharma, N. Arul Dhas, K. C. Patil, *Mat. Sci. Engin.* B40 (1996) 153.
[115] M. Yoshimura. *Ceram. Bull.* 67 (1988) 1950.
[116] J. D. Lin, J. Q. Duh, *J. Mat. Sci.* 32 (1997) 4901; *J. Mat. Sci.* 32 (1997) 5779; *J. Am. Ceram. Soc.* 81 (1998) 853.
[117] D. G. Lamas, A. M. Rosso, M. Suárez Anzorena, A. Fernández, M. G. Bellino, N. E. Walsöe de Reca, A.F. Craievich, *Activity Rep. Brazi. Synchr. Light Lab.*, (2004) paper 453. Ed. in CD.
[118] D. G. Lamas, A. M. Rosso, M. Suárez Anzorena, A. Fernández, M. G. Bellino, M. D. Cabezas, N. E. Walsöe de Reca, A. F. Craievich, *Script. Mat.,* **55** (2006) 553-556.
[119] K. Yardley. *Mineralog. Mag.* 2 (1926) 169.
[120] M. Yoshimura, *Ceramic Bulletin,* 67 (1988) 1950.
[121] D. K. Smith, H. W. Newkirk, *Acta Cryst.* 18 (1963) 983.
[122] G. Teufer, *Acta Cryst.* 15 (1962) 1187.
[123] A. Chatterjee, S. K. Pradhan, A. Datta, M. D. Chakravorty, *J. Mat. Res.,* 9 (1994) 263.
[124] B. E. Yoldas. *J. Am. Ceram. Soc.*, 65 (1982) 387.
[125] A. Clearfield, *Inorg. Chem.*, 3 (1964) 146.
[126] K. S. Mazdiyasni, C. T. Lynch, J. S. Smith. *J. Am. Chem. Soc.* 49 (1966) 286.
[127] G. Stefanic, S. Popovic, S. Music. *Thermochim. Acta*, 303 (1997) 31.
[128] S. Roy, J. Ghose. *Mater. Res. Bull.*, 35 (2000) 1195.
[129] H. G. Scott. *J. Mat. Sci.* 10 (1975) 1257.
[130] D.G. Lamas and N.E. Walsöe de Reca, *Mat. Lett.* 41 (1999) 204.
[131] D. G. Lamas, G. E. Lascalea, R. E. Juárez, M. F. Bianchetti, M. E. Fernández de Rapp, N. E. Walsöe de Reca, Proceed. *CONAMET-SAM/ Symposium Materia,* Santiago, Chile, 12-15th. Nov. 2002, Vol. II, 659. Publish. by the Latinam. Materials Rev. 'Materia' 8 (2003) 213.
[132] R. O. Fuentes, D. G. Lamas, I. O. Fábregas, M. E. F. Rapp, N. E. Walsöe de Reca, A. F. Craievich, M. C. A. Fantini. *Adv. in X-Ray Techn. Analysis,* Vol. XIII, *Proceed. IX Latinam. Seminar for X-Rays Techniques Analysis*, SARX, (2004).
[133] C. F. Grain, *J. Am. Ceram. Soc.* 50 (1967) 288.
[134] V. S. Stubican, S. P. Ray. *J. Am. Ceram. Soc.* 60 (1977) 534.
[135] P. Durán, M. González, C. Moure, J. R. Jurado, C. Pascual. *J. Mat. Sci.* 25 (1990) 5001.
[136] R. E . Juárez, D. G. Lamas, G. E. Lascalea, N. E. Walsöe de Reca, Proceed. *"X Congr. Intern. de Cerám., Vidrio y Refract." - "V Congr. de Cerám. del Mercosur"*, San Martín, 18-20th. Sept. 2000) 43.
[137] G. E. Lascalea, D. G. Lamas, E. Djurado, N. E. Walsöe de Reca, *Proceed. of the "22nd RISÆ Interna. Symp. on Mat. Sci."* (Roskilde, Denmark, 3-7th. Sept. 2001) 313.
[138] A. Trovareli, Ed. *"Catalysis by Ceria and Related Materials"* (2002) London, Imperial College Press.
[139] *P. Heitjans, S. Indris, J. Phys.: Condens. Matter*, 15 (2003) 1257.
[140] H. L. Tuller, *Solid State Ionics,* 131 (2000) 143.

[141] A. V. Chadwick, in *Proc. Diffusion Fundamentals Leipzig 2005,* Eds. J. Kärger, F. Grinberg, P. Heitjans, Leipziger Universitätsverlag, Leipzig, Germany (2005) 204-225.

[142] I. Kosacki, T. Suzuki, V. Petrovsky, H. U. Anderson, *Solid State Ionics,* 136 (2000) 1225.

[143] T. Suzuki, I. Kosacki, H. U. Anderson, *Solid State Ionics*, 151 (2002) 111.

[144] S. Jiang, W. A. Schulze, V. R. W. Amarakoon, G. C. Stangle, *J. Mater. Res.*, 12 (1997) 2374.

[145] Y. M. Chiang, E. B. Lavik, D. A. Blom, *Nanostruct. Mater.*, 9 (1997) 633.

[146] V. V. Kharton, F. M. Marques, B. A Atkinson, *Solid State Ionics,* 174 (2004) 135.

[147] A. K. Jonscher, *Nature*, 267 (1977) 673.

[148] A. Dutta, A.Ghosh, *Phys. Review B.* Cond. Matter.Phys., 72 (2005) 24.

[149] A. S. Nowick, W. K. Lee, in *"Superionic Solids and Solid Electrolytes"*- Recent Trends. Ed. A. L. Laskar, S. Chandra, Academic Press, London (1989).

[150] G. J. Dienes, *J. Appl. Phys.*, 21 (1950) 1189.

[151] C. R. Mariappan, G. Govindaraj, *Physica B,* 353 (2004) 65.

[152] C. R. Mariappan, G. Govindaraj, L. Ramya, S. Hariharan, *Mater. Res. Bull.*, 40 (2005) 610.

[153] N. M. Vijayakumar, S. Selvasekarapandian, M. S. Bhuvaneswari, G. HiranKumar, G. Ramprasad, R. Subramanian, P. C. Angelo, *Physica B,* 334 (2003) 390.

[154] K. Funke, *Prog. Solid State Chem.*, 22 (1993) 111.

[155] J. Philibert, *Atom Movements Diffusion and Mass Transport in Solids*. Ch. IV, EDP Sciences, Les Ulis, France (1991).

[156] D. P. Almond, A. R. West, *Solid State Ionics,* 18-19 (1986)1105-1109.

[157] A. S. Nowick, B. S. Lim, *Phys. Rev. B*, 63 (2001)184 115.

[158] J. R. Mac Donald, *Solid State Ionics,* 133 (2000) 79-82.

[159] D. P. Almond, G. K. Duncan, A. R. West, *Solid State Ionics,* 8 (1983) 159.

[160] B. C. H. Steele, *Solid State Ionics*, 129 (2000) 95.

[161] X. Guo, R. Waiser, *Prog. Mater. Sci.* 51 (2006) 151.

[162] L. M. Hodge, M. D. Ingram, A. R. West, *J. Electroanal. Chem.* 74 (1976) 125.

[163] G. J. Dienes, *J. Appl. Phys.* 1950, *21*, 1189.

[164] N. Yamazoe, J. Fuchigami, M. Kishikawa, T. Seiyama, *Surf. Sci.* 86 (1979) 335.

[165] Y. Shimizu, M. Egashira, *MRS Bulletin*, 24, 6 (1999) 18.

[166] C. Xu, J. Tamaki, N. Miura, N. Yamazoe, *Sens. & Actuators*, B 3 (1991) 147.

[167] M. Cabezas, R. Baby, E. Cabanillas, D. Lamas, N. E. Walsöe de Reca. Application for *A. R. Patent* of a sensor (in process).

[168] M. F. Bianchetti, M. E. F. de Rapp, R. E. Juárez, N. E. Walsöe de Reca, Application for *A. R. Patent* (in process).

[169] M. F. Bianchetti, N. E. Walsöe de Reca. Application for *A. R. Patent* (in process).

[170] M. F. Bianchetti, N. E. Walsöe de Reca. Application for *A. R. Patent* of a sensor (in process).

[171] V. Foglietti, A. Bearzotti, P. Degasperis, S. Petrocco, R. Angelucci, G. Cardinali, L. Dori, P. Maccagnini, A. Parisini, A. Poggi, M. Severi, M. Carrozza, P. Dario, B. Magnani, A. Menciassi, *Annual Report-* Consiglio delle Richerche, LAMEL, (1997) 63.

[172] G. Cardinali, L. Dori, M. Fiorini, I. Sayago, G. Faglia, C. Perego, G. Sverveglieri, V. Liberati, F. Maloberti, D. Tonietto, *Annual Report,* Consiglio delle Richerche, LAMEL (1998) 71.

[173] L. T. Alaniz, C. L. Arrieta, M. F. Bianchetti, C. A. Gillari, J. F. Giménez, H. A. Lacomi, D. F. Valerio, N. E. Walsöe de Reca, *AR patent* N° P-070105987 granted on December 20th, 2007.

[174] D. G. Lamas, L. Fraigi, N. E. Walsöe de Reca, Application for *A. R. Patent* (in process).

[175] B.C.H. Steele, *Nature,* 400 (1999) 619.

[176] E. Perry Murray, T. Sai, S. A. Barnett S.A., *Nature,* 400 (1999) 649.

[177] S. Park, J. M. Vohs, R. J. Gorte, *Nature,* 404 (2000) 265.

[178] T. Hibino, S. Wang, S. Kakimoto, M. Sano, *Solid State Ionics*, 127, 2000, 8.

[179] T. Hibino, A. Hashimoto, T. Inoue, J. Tokuno, S. Yoshida, M. Sano, *Science*, 288, 2000, 231.

[180] T. Hibino, A. Hashimoto, T. Inoue, J. Tokuno, S. Yoshida, M. Sano, *J. Electrochem. Soc.,* 147, 2000, 2888.

[181] T. Hibino, A. Hashimoto, M. Yano, M. Suzuki, S. Yoshida, M. Sano M., *J. Electrochem. Soc.*, 149 (2002) A133.

[182] A. Tomita, D. Hirabayashi, T. Hibino, M. Nagao, M. Sano, *Electrochem. Solid-State Lett.*, 78, 2005, A63.

[183] T. W. Napporn, F. Morin, M. Meunier, *Electrochem. Solid-State Lett.*, 7, 2004, A60.

[184] T. W. Napporn, X. Jacques-Bédard, F. Morin and M. J. Meunier, *Electrochem. Soc.*, 151 (2004) A2088.

[185] M. D. Cabezas, D. G. Lamas, M. G. Bellino, R. O. Fuentes, N. E. Walsöe de Reca, *ECS Transactions - Solid Oxide Fuel Cells,* 7 (2007) 955.

[186] I. Ruiz de Larramendi,D. Lamas, A. Fernández, J. I. Ruiz de Larramendi,T. Rojo, N. E. Walsöe de Reca,*ECS Transactions, Solid Oxide Fuel Cells*, 7 (2007) 1147.

[187] A. Boudghene Stambouli, E. Traversa, *Renew. Sust. Energy Rev.* 6 (2002) 433.

[188] A. Trovarelli, *Cat. Rev. Sci. Eng.* 38 (1996) 439.

[189] M. Bellino, J. Sacanell, D. Lamas, A. G. Leyva, N. E. Walsöe de Reca, *ECS Transactions. Solid Oxide Fuel Cells,* 7 (2007) 1299.

[190] M. Mogensen, in "Catalysis by ceria and related materials", edited by A. Trovarelli, Ed. Imperial College Press, London, 2002, 453.

Manuscrito recibido el 8 de abril de 2008.
Aceptado el 12 de mayo de 2008.